nature communications

Article

https://doi.org/10.1038/s41467-025-67092-x

Alternative antigen retention by a gp96-fusion approach induces long-lasting and broad immunity in mice

Received: 19 February 2025

Accepted: 18 November 2025

Published online: 17 December 2025

Check for updates

Fang Cheng[1,2,5], Baifeng Wang[1,2,5], Xinran Zhu[1,2,3,5], Zihao Wang[1,2], Haoyu Wang[1,2], Rui Li[1,2], Chan Xing[1,2], Ying Ju[1], Rongguo Wei[1,4] ✉, Xin Li[1] ✉ & Songdong Meng[1] ✉

Efficient antigen delivery to B cells and dendritic cells (DC) is critical for enhancing vaccine immunogenicity. Here, we develop a dimeric vaccine strategy by fusing antigens to the N-terminal of heat shock protein GP96. This platform generates compact, nanoscale particles that fully exposed antigenic sites. We validate the vaccine strategy using the SARS-CoV-2 receptor-binding domain (RBD) antigen in a viral challenge model with hACE2 mice and the human papillomavirus (HPV) E7 protein in a HeLa xenograft model with nude mice. The GP96 moiety directly bound its receptor, LRP1, thereby enhancing antigen accumulation on follicular DCs and prolonging lymph node retention, ultimately amplifying germinal center B cell responses. Furthermore, GP96-LRP1 interaction on DCs promotes antigen endocytosis, underpinning epitope presentation and robust cross-conserved T cell activation. Consequently, this design induces potent, durable humoral immunity, cross-conserved T cell responses, and pulmonary mucosal immunity, underscoring its promise as a versatile and effective vaccination strategy.

Effective vaccines against continuously emerging and mutating viruses such as SARS-CoV-2 and influenza are challenging to design, and existing vaccines have limited efficiency[1,2]. The primary concerns are the limited cross-protection and transient nature of the antibody response elicited by the vaccines[3]. Additionally, while T cells are pivotal in viral clearance and confer long-lasting protection, current vaccination strategies have encountered difficulties in mounting effective T cell responses[4]. The lack of robust antiviral T cell immune response also limits existing vaccine utility against chronic viral infections such as HPV. Novel vaccination approaches are being actively investigated, which include the utilization of diverse adjuvants, nanoparticle-based antigen delivery systems, artificial intelligence (AI) aided vaccine design, the advancement of mRNA-based or viral vector vaccines, and the engineering of vaccines capable of inducing a more extensive and enduring B cell and T cell response[5–9]. Adjuvants strengthen and prolong the immune response by facilitating antigen depot formation, prolonging antigen exposures and release, stimulating innate immunity, and enhancing antigen presentation[10,11]. The emergence of SARS-CoV-2 variants has complicated the efficacy of current vaccines; however, long-term persistence of neutralizing antibody responses and the diversity and cross-reactivity of T cell responses may serve to ameliorate the clinical impact of these variants[12–14]. Therefore, vaccine development must prioritize strategies to maintain long-term antibody response as well as the induction of sustained, cross-protective T cell responses through revolutionizing adjuvant development.

Heat shock protein GP96/GRP94, a member of the heat shock protein 90 (HSP90) family, is a pivotal molecular chaperone located

[1]CAS Key Laboratory of Pathogen Microbiology and Immunology, Institute of Microbiology, Chinese Academy of Sciences (CAS), Beijing, China. [2]University of Chinese Academy of Sciences, Beijing, China. [3]Tongliao Center for Animal Disease Control and Prevention, Tongliao, China. [4]Department of Clinical Laboratory, The Fifth Affiliated Hospital of Guangxi Medical University, Nanning, Guangxi, China. [5]These authors contributed equally: Fang Cheng, Baifeng Wang, Xinran Zhu. ✉e-mail: unwrong@126.com; lix@im.ac.cn; mengsd@im.ac.cn

within the cellular endoplasmic reticulum (ER). GP96 has emerged as a subject of intense scrutiny in immunological research, with its potential as a vaccine adjuvant to activate T-cell responses being particularly promising[15,16]. Its ability to complex with a diverse array of MHC class I and class II epitopes, forming GP96-peptide complexes, is crucial for the cross-presentation to $CD8^+$ T cells, a process integral to cellular immune responses[17]. Additionally, GP96 also stimulates the production of cytokines and chemokines via interaction with CD91 (LRP1) and Toll-like receptors (TLR), thereby inducing the maturation of dendritic cells and macrophages[18]. The application of GP96 as an adjuvant in split influenza vaccine indicates its potential to elicit protective T cell immune responses against various strains of the influenza virus[19]. In the realm of tumor immunotherapy, tumor-derived GP96-peptide complexes activate $CD8^+$ T cells by presenting tumor-specific antigens, offering novel and safe strategies for clinical cancer treatment[20,21]. Despite the notable advancements in GP96 immunological function, the precise form of antigen binding by GP96 remains to be fully elucidated, and its relatively weak ability to promote B-cell responses potentially limits its application in vaccine strategies[22].

Given the uncertainty surrounding the binding of large antigens to GP96, we adopt a fusion protein strategy to redesign the antigen-GP96 complex using a structure-based approach[23–25]. In this study, we construct antigen-GP96 fusion proteins using the RBD of the SARS-CoV-2 spike protein and the L1 and E7 proteins of HPV. Their immunogenicity is compared with that of established adjuvants, including aluminum salts, MF59, AS04C, and AS04D. The results demonstrate that this vaccine strategy induces potent humoral immunity, cross-protective T cell responses, and pulmonary mucosal immunity. These findings establish a novel vaccine platform for developing highly effective and broad-spectrum vaccines against diverse pathogens.

Results

Structure-guided design of a dimeric form of RBD-GP96-Fusion as a superior immunogen

Screenings related to different antigen-GP96 binding modes were first carried out in light of the adjuvant characteristics of GP96. The binding of multiple viral antigens was simulated using AlphaFold3, including SARS-CoV-2 RBD, FluA HA1, HPV L1, HBV HBc, HIV gp120, MPXV B6R and M1R, HFMD CA16 and EV71, and OVA, whose molecular weight is mainly concentrated within the range of 35 to 50 kDa. And the modeling results are corrected for deviations and subjected to orthogonal experiments to ensure their rationality (Supplementary Fig. 1). After large-scale screening and statistical analysis, it was found that these antigens tended to predominantly bind to the N-terminal domain (NTD), and secondly to the middle domain (MD) of GP96 (Fig. 1A, B, and Supplementary Fig. 1, 2A). Therefore, fusing the antigens to the N-terminal of GP96 is more conducive to reducing the spatial hindrance between the antigens and GP96, further ensuring the integrity of the recombinant protein structure and the full exposure of the antigens. Moreover, we analyzed the GP96 binding sites with different subtype antigenic MHC class I/II epitopes that are usually less than 30 aa. The results show that the GP96 dimer uses its lumenal channel formed within its MD and C-terminal domain (CTD) to bind various viral epitope peptides for cross-presentation and induce T cell immune responses (Supplementary Fig. 2B), which is in line with previous reports[26].

Unlike epitope peptides, the viral antigens (such as RBD and L1 protein), which are much larger in size, were unable to form stable complexes with GP96 protein (Supplementary Fig. 2C). This offers a valuable reference for our subsequent design of the antigen-GP96-Fusion vaccine strategy. The mature GP96 protein contains a flexible region (aa 22-45) at the N-terminal that could be used as a natural linker to allow RBD to interact with NTD. Additionally, by leveraging the dimerization characteristic of both the C-terminal of GP96 and RBD, a more stable RBD-GP96 fusion protein with dimerization at both the N- and C-terminal will be formed. The RBD is truncated at the C-terminal residue G545 and connected with GP96 protein N-terminal residue D22 to construct fusion protein (Fig. 1C). Molecular dynamics simulation results indicate that the root mean square deviation (RMSD) fluctuations of the RBD-GP96-dimer tend to be more stable compared to the GP96-dimer (Fig. 1D). The flexibility of Chain A and Chain B of GP96 dimer decreased when combined with RBD, particularly for Chain B (Supplementary Fig. 3A). The snapshot of the last frame of the dynamics simulation was then intercepted to represent a more reasonable conformation of the GP96 and RBD-GP96 dimer complex for further analysis. After RBD was coupled to its N-terminal, a large number of hydrogen bonds were formed between RBD Chain A/B and GP96 Chain A/B, further facilitating the stability of the N-terminal of the dimer (Fig. 1E, and Supplementary Fig. 3B). Then recombinant RBD-GP96-Fusion was expressed, and its molecular weight was determined to be 231 kDa through analytical gel filtration and analytical ultracentrifugation, suggesting stable dimer formation (Fig. 1F, G). Transmission electron microscopy observations show that the dimerization of RBD-GP96-Fusion is more compact at both the N- and C-termini compared to GP96 (Fig. 1H). Based on the analysis of the mass spectrometry results regarding the positioning information of disulfide bonds, disulfide bonds are formed mutually between Cys258 (Chain A) - Cys258 (Chain B) of the two RBDs among partial RBD-GP96-Fusion proteins, further facilitating the formation of dimerization conformations: “closed” conformation at the N-terminus through a disulfide bond, and “open” conformation at the N-terminus with no disulfide bonds (Fig. 1I, and Supplementary Fig. 4). Two different twisted models of RBD-GP96-Fusion are consistent with the results of structural predictions.

The surface plasmon resonance (SPR) and ELISA assays indicated that the RBD-GP96-Fusion bound to the SARS-CoV-2 receptor hACE2 with an affinity comparable to the RBD dimer counterpart (Fig. 2A, and Supplementary Fig. 5A). This implies the exposure of the receptor binding motif (RBM), which is in accordance with the results of multiple structural predictions (Fig. 2B, Supplementary Fig. 5B). The aggregation temperatures (Tagg) of GP96 and RBD-GP96-Fusion were significantly higher than that of RBD (Fig. 2C, Supplementary Fig. 6A). Meanwhile, the anti-trypsin enzymatic cleavage ability of GP96 or RBD-GP96-Fusion was significantly enhanced compared to RBD alone (Fig. 2D). Obviously, the enhanced stability of RBD-GP96-Fusion is majorly dependent on the properties of GP96. The results of the in vivo stability study showed that the duration for RBD-GP96-Fusion to exist stably, acting like a sustained-release depot, at the injection site on the backs of mice and subsequently in the inguinal lymph nodes was significantly prolonged compared to that of RBD and GP96 proteins (Fig. 2E). A larger amount of fluorescently labeled RBD was captured by the inguinal lymph nodes (LN) as early as 3 h after the subcutaneous injection of RBD-GP96-Fusion, and the majority of the RBD antigen persisted within the lymph nodes and spleen for at least 30 days.

RBD-GP96-Fusion vaccine promotes the generation of potent neutralizing antibodies via activation of GC B cell response

To evaluate humoral responses, BALB/c mice were immunized three times with RBD-GP96-Fusion or RBD immunogen plus alum or GP96 adjuvant as controls (Fig. 3A). The antibody response to RBD-GP96-Fusion is dose-dependent, and a sufficient high-titer antibody can be produced when immunized with 20 μg of protein (Supplementary Fig. 7A). The inoculation dosage of 20 μg RBD-GP96-Fusion protein was used in the following experiment. The dose of 5 μg of RBD was then used for inoculation in the control groups to maintain the same molar amount of RBD immunogen as in RBD-GP96-Fusion group[11]. Compared to the RBD with alum or GP96, the RBD-GP96-Fusion of prototype SARS-CoV-2 induced significantly higher levels of antigen-specific IgG, IgG1, IgG2a, IgG2b and IgM, and no obvious increases in IgA and IgE levels were observed in serum (Fig. 3B, and Supplementary Fig. 7B-E). The mean IgG titer under RBD-GP96-Fusion treatment was

https://doi.org/10.1038/s41467-025-67092-x

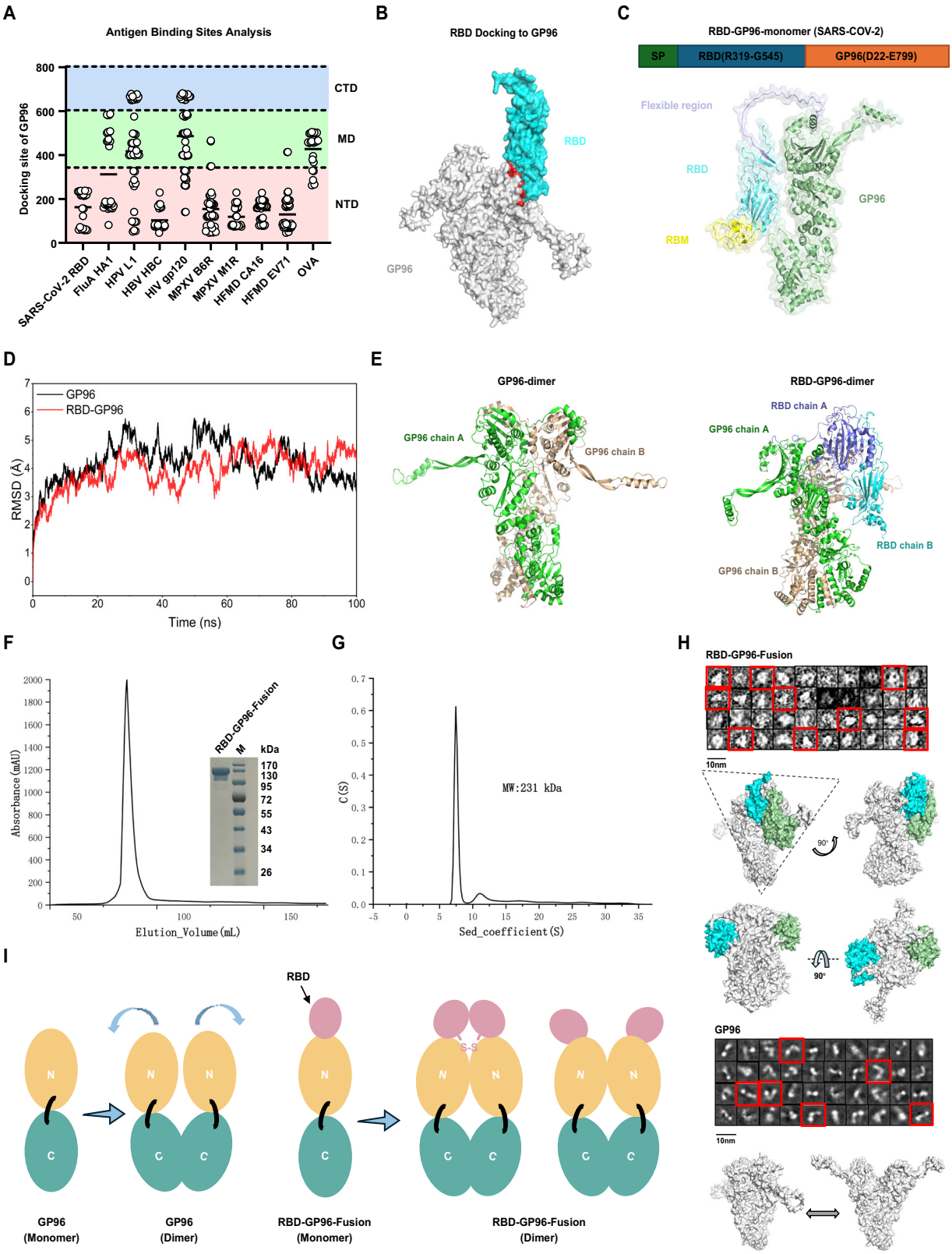

up to 63 times higher than that of alum after the 3rd immunization, which persisted for 6 months. In terms of cross-antibody reactions against different SARS-CoV-2 strains of RBD and S1 subunit, RBD-GP96-Fusion immunity was significantly stronger than other treatments (Fig. 3C, D). We found that RBD-GP96-Fusion could induce a strong antibody-dependent cellular cytotoxicity (ADCC) reporter activity in mouse cells (Fig. 3E)[27,28].

We then detected the major inflammatory cytokines in the plasma. As seen in Supplementary Fig. 7F, only a modest increase in IFN-γ and TNF levels was observed after the third immunization of RBD-GP96-Fusion relative to alum adjuvant, suggesting that it did not trigger a systemic inflammatory response[11]. We also monitored the weight change curves of mice throughout the entire vaccination period and did not observe any significant weight loss under RBD-GP96-

Fig. 1 | Structure-guided design and critical structure characterization of antigen-GP96-fusion strategy: RBD-GP96-Fusion as an instance. A Large-scale analysis of the key binding regions of antigens with GP96 using AlphaFold3 ($n = 22$). **B** The possible structural pattern diagram of the combination of RBD and GP96 modeled by AlphaFold3. **C** The schematic representation of RBD-GP96-Fusion (monomer). RBDs (prototype strain) are truncated at the C-terminal residue G545 and connected to GP96 protein N-terminal residue D22 to construct the fusion protein (SP, signal peptide). The structure of the fusion protein was predicted based on AlphaFold3 (yellow RBM motif, hACE2 binding domain). **D**, **E** Molecular dynamics of GP96-dimer and RBD-GP96-dimer predicted by AlphaFold2-multimer were performed using AMBER. **D** The RMSD was analyzed. The red line represents RBD-GP96-dimer and the black line represents GP96-dimer. **E** The last frame of the molecular dynamics operation of the dimer conformations is captured for display. **F** Analytical gel filtration of the RBD-GP96-Fusion protein was performed with Superdex 200 Increase 10/300 GL. The resulting 280-nm absorbance curve is shown. The reduced SDS-PAGE migration profile of the pooled sample is shown. The data are representative of two independent experiments with similar results. **G** Ultracentrifugation sedimentation profiles of RBD-GP96-Fusion. **H** Transmission electron microscopy of RBD-GP96-Fusion and GP96 protein. The red frames represent typical transmission electron microscopy (TEM) structures. Below is a 3D cartoon sketch of the RBD-GP96-Fusion (surface, cone). **I** Analysis of GP96 and RBD-GP96-Fusion dimerization models.

Fusion treatment (Supplementary Fig. 7G). No other apparent toxicity was found.

In terms of vaccine protection efficacy, all serum samples from the RBD-GP96-Fusion group also exhibited a much higher neutralizing activity against both live prototypic and Omicron BA.1 strains, with approximately a 63-fold and 4-fold increase, respectively, compared to alum (Fig. 3F, and Supplementary Fig. 7H, I). Additionally, neutralizing antibody (NAb) titers demonstrated a stronger correlation with IgG titers (Supplementary Fig. 7J). We further applied this N-terminal fusion strategy to reconstitute the SARS-CoV-2 XBB.1.5 RBD-GP96-Fusion vaccine for immunization (Supplementary Fig. 8A). Similar to the prototypic RBD, the XBB.1.5 RBD-GP96-Fusion generated stronger antigen-specific IgG and NAbs (Fig. 3G, and Supplementary Fig. 8B), and the NAb titers against Omicron BA.1 were enhanced significantly (Supplementary Fig. 8C). After immunization of hACE2 transgenic mice, a nasal SARS-CoV-2 XBB.1.22 challenge test was conducted. The RBD-GP96-Fusion group showed significantly better protective effect than RBD plus alum group, with the lower viral titer in the lungs and no signs of severe bronchopneumonia or interstitial pneumonia in the pathological sections (Fig. 3H–J). Then we compared bone marrow SARS-CoV-2-specific Ab-secreting cells (ASC) elicited by the different vaccines 6 months post-immunization. Consistent with the serum IgG data, mice immunized with prototypic or XBB.1.5 RBD-GP96-Fusion but not RBD plus alum or GP96 generated RBD-specific IgG^+ long-lived plasma cells (LLPC) (Fig. 3KL), suggesting efficient generation of multiple facets of long-term humoral immunity by RBD-GP96-Fusion vaccines. Notably, the RBD-GP96-Fusion barely produces antibodies against its own GP96 (Supplementary Fig. 8D).

We then proceeded to investigate the immune cell repertoire bound by RBD-GP96-Fusion protein via flow cytometry and single-cell RNA sequencing (scRNA-seq), as illustrated in Supplementary Fig. 9A. As shown in Supplementary Fig. 9B,C, RBD-GP96-Fusion protein accumulates significantly more at the draining lymph nodes of the mice. Among $Cy5^+$ cells, we initially grouped the scRNA-seq data into 8 cell clusters, including clusters of B cells, T cells, monocytes, etc., to provide an analytical framework for further in-depth refinement (Supplementary Fig. 9D, E).

Next, we subclustered B cells and obtained 5 subsets according to the expression of canonical B cell markers[29–31] (Supplementary Figs. 10A, B). As seen in Fig. 3 M-N, compared with the RBD control group, the RBD-GP96 fusion protein was most bound to germinal center (GC) B cells. The enrichment of functional modules of differentially expressed genes (DEG) in the various cell types indicated that the shared upregulation module was predominantly enriched in GC B cells, and was focused on amino acid metabolism as well as formation of immunological synapse with antigen-presenting cells (APC) (Supplementary Figs. 10C, D).

Subsequently, GC B cells from the draining inguinal LNs were assessed 7 days post-immunization by flow cytometry (Fig. 3O). The RBD-GP96-Fusion immunization significantly induced a higher frequency and quantity of GC B cells and antigen-specific GC B cell responses compared to alum or GP96 (Fig. 3P, Q and Supplementary Fig. 11A). The same GC B cell responses were maintained but slightly diminished on day 40 (Supplementary Fig. 11B). To understand the long-term efficacy of antibody levels further, we measured GC memory B-cell (MBC) precursors (as defined in Supplementary Fig. 11C) in the inguinal LNs 7 days post-immunization. We found that a substantial population of RBD-specific MBC precursors was present only upon immunization with RBD-GP96-Fusion vaccines (Fig. 3R, and Supplementary Fig. 11A). MBCs were measured in the spleen of mice 6 months after vaccination. RBD-GP96-Fusion vaccines promoted the generation of class-switched MBCs expressing IgG1 and IgG2a/2b, but no significant difference was observed in RBD specificity[7,32] (Fig. 3S, and Supplementary Fig. 11D, E). The immunization with XBB.1.5 RBD-GP96-Fusion is also consistent with the GC responses mentioned above (Supplementary Fig. 11F–H). To better study MBCs and MBC precursors, the formation of MBCs was analyzed 8 weeks after the third immunization, that is, after the GC collapse. At this time, the differences in MBC precursors were no longer significant, and the differences in memory cells were more concentrated on the high-intensity IgG1 and IgG2a/b MBCs. The progress of the promoting kinetics conforms to the above-mentioned GC transformation (Supplementary Fig. 12).

After analyzing the above immune response, it was found that the quantity of RBD-GC B cells shows a strong correlation with IgG and NT50 titer at different immunization stages (Supplementary Fig. 13A–C). Regarding the maintenance of antibodies, the strong correlation between RBD-specific ASCs and long-lasting antibodies in the RBD-GP96-Fusion group also demonstrated its superiority (Supplementary Fig. 13D).

Besides BALB/c mice, induction of humoral response by RBD-GP96-Fusion was also determined in C57BL/6 background mice[33]. Despite a somewhat weakened humoral response compared to BALB/c mice, RBD-GP96-Fusion induced significantly stronger antibody response and GCB-related reactions than those of alum or GP96 adjuvant control in HLA-A2(Kb)/B6 transgenic mice (Supplementary Fig. 14).

The RBD-GP96-Fusion vaccine generates an alternative antigen retention route via LPR1 on FDCs for continuous activation of GC B cells

Then we subclustered monocyte cells and obtained 6 subsets according to the expression of canonical cell markers[34] (Supplementary Fig. 15A, B). There was a significant increase in RBD-GP96-Fusion protein-bound follicular dendritic cells (FDC) compared to RBD control (Fig. 4A, B). The enrichment of functional modules of DEGs indicated the upregulation of cytokine-mediated signaling and regulation of cell-cell adhesion (Supplementary Fig. 15C), suggesting that the RBD-GP96-Fusion protein promotes direct or indirect interactions between FDCs and targeted cells.

FDCs are dynamic antigen libraries in the GCs, providing the first signal for activating GC B cells[35–37]. T follicular helper (Tfh) cells can provide the second signal for activating GC B cells by secreting corresponding cytokines[7]. There were no significant differences in the frequency, quantity, and activation of Tfh cells between the RBD-GP96-Fusion group and the groups with RBD with alum or GP96 overall

https://doi.org/10.1038/s41467-025-67092-x

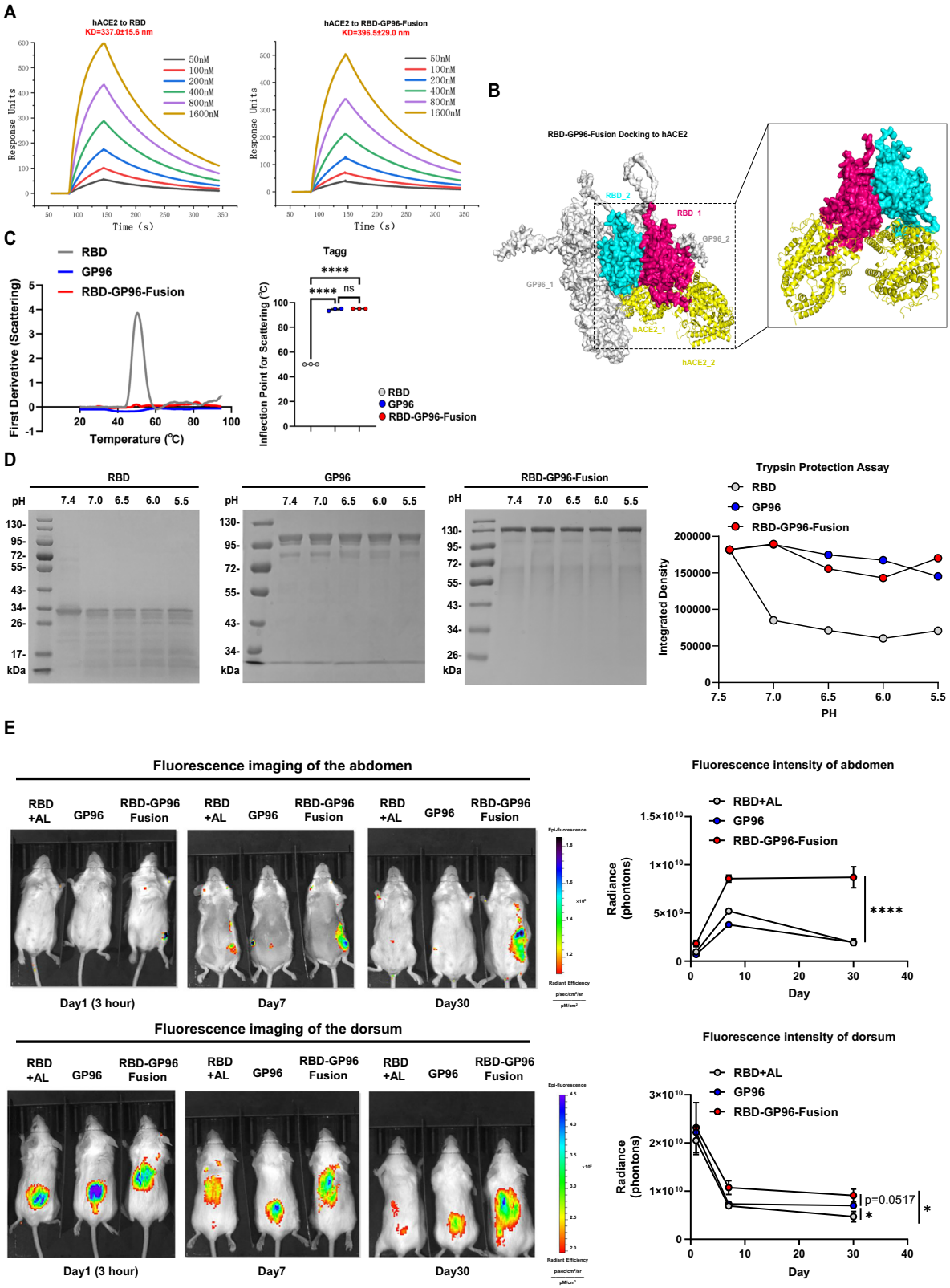

(Supplementary Fig. 16). A relatively higher percentage of IFN-γ$^+$ or IL-4$^+$ Tfh was observed in the RBD-GP96-Fusion group under stimulation with PMA/Ionomycin or RBD peptide pool. FDCs have the unique ability to retain intact antigen for extended periods. They primarily bind antigen-immune complexes onto the cell membrane via surface Fc fragment receptor (FcR) and complement receptor 2 / complement receptor 1 (CR2/CR1), and subsequently present them to B cells. FDCs were evaluated in inguinal LNs 7 days post-immunization by flow cytometry[38,39] (Supplementary Fig. 17A). In the RBD-GP96-Fusion group, the frequency of RBD-GP96-Fusion-specific FDCs exceeded that of RBD-specific FDCs in the RBD with alum group by around 1.3-fold. Furthermore, even after applying FcR blocking inhibitors, the disparity persisted (Fig. 4C, Supplementary Fig. 17B). This indicates that aside from the classical antigen retention pathways involving FcR

Fig. 2 | Biological stability and immunological migration characteristics of RBD-GP96-Fusion as a dominant vaccine. A Representative BIAcore diagrams of RBD and RBD-GP96-Fusion bound to hACE2 protein (baculovirus expression). The K_D value was calculated using the software BIAevaluation Version 4.1 (GE Healthcare). The values shown are mean ± SD of two independent experiments. **B** The complex structure of hACE2 (PDB: 1R42) is docked onto RBD-GP96-Fusion dimer by ZDOCK, showing the complete exposure of dual RBMs. Two RBD protomers are shown as surface and colored in hot pink and cyan, respectively. Two hACE2 proteins are shown as cartoon and colored in yellow. **C** The difference in thermal aggregation degree between RBD, GP96 and RBD-GP96-Fusion proteins was analyzed using the PR.NT.48 instrument. **D** The SDS-PAGE migration profiles of RBD, GP96 and RBD-GP96-Fusion hydrolyzed by trypsin at different pH were analyzed to determine the difference in anti-enzymatic ability. **E** Representative in vivo fluorescein image of 6- to 8-week-old female BALB/c mice on days 0, 7, and 30 after dorsal vaccination with RBD (with aluminum hydroxide adjuvant), GP96 and RBD-GP96-Fusion vaccines. In (**C**, **E**), $n = 3$ samples per group were analyzed. The data are representative of two independent experiments with similar results. Geometric mean ± geometric SD are shown. One-way ANOVA with Bonferroni correction or unpaired two-tailed t tests were conducted according to the distribution of the data. ns p å 0.05, $^{*}p \le 0.05$, $^{****}p \le 0.0001$.

and CR2, the RBD-GP96-Fusion antigen can be retained on the surface of FDC through other routes.

We postulate that there may exist GP96-related receptors on the surface of FDCs, enabling RBD-GP96-Fusion to anchor the antigen more abundantly on the surface of FDCs via GP96[40–42]. The results of flow cytometry indicated that both TLRs and LRP1 were expressed on the surface of FDCs (Fig. 4D). Then, FDCs were evaluated in LNs 7 days post-immunization. The combination of FcR blocking, TLR mAb, and LRP1 mAb inhibitors was employed to detect the frequency variations of antigen-specific FDCs. The results revealed that blocking both FcR and LRP1 mostly decreased the binding of the RBD-GP96-Fusion antigen to FDCs, and the combination blocking almost completely inhibited the binding (Fig. 4E–G, and Supplementary Fig. 17C). However, only blocking FcR, not LRP1, significantly decreased the binding of RBD to FDCs. Similar to the binding to FDCs, the results of in vivo immune experiments in mice also demonstrated that LRP1 blocking led to a significant reduction in IgG titers (Fig. 4H, I). After the first immunization, the lymph nodes were extracted and ground, and FDCs were sorted for RBD IP-Western analysis (Fig. 4J, Supplementary Fig. 17D). Likewise, for the unimmunized lymph nodes, FDCs were sorted and incubated with various proteins before undergoing RBD IP-Western analysis (Fig. 4K). The in vivo and in vitro results both indicated the existence of the RBD-GP96-Fusion-LRP1 complex on the surface of FDCs. After one immunization, the lymphocyte suspension was used for Protein A/G beads to directly bind B cells' BCR and perform IP-Western blot. The results directly proved that B cells and FDCs were bound by the RBD-GP96-Fusion mediated by LRP1 (Fig. 4L).

Next, we assessed the ability of in vitro RBD-GP96-Fusion-stimulated FDCs to prolong the interaction with GC B cells, as measured by time-lapse live-cell microscopy. Figure 4M shows representative FDC-GC B interactions over time. The interaction time between FDCs and GC B cells was significantly enhanced by RBD-GP96-Fusion, and could be blocked by LRP1 antibodies (but not by an isotype control antibody) (Fig. 4N, O). Additionally, after immunization, the frequency of RBD-GP96-Fusion-bound FDCs and GC B cells in the LNs was significantly higher than RBD-bound cells in the alum adjuvant group (Fig. 4P, and Supplementary Fig. 18).

From a structural perspective, AlphaFold3 was utilized to model and analyze LRP1/CD91α. Based on research conducted by Robert J. Binder, we determined that the free GP96 subunit binds to CD91-α through a structural proline-cleavage site to evaluate the feasibility of the vaccine conformation[40] (Supplementary Fig. 19). Subsequently, GP96 and RBD-GP96-Fusion were docked with CD91-α for analysis. The results revealed that the docking sites were all situated on the free subunit, suggesting that the docking results merit consideration (Supplementary Fig. 20). At this point, the proposed solution is feasible, as indicated by the fully exposed RBM in RBD (Fig. 4Q). To enhance the structural platform's subsequent application potential, we analyzed the CD91α-GP96 binding interface via molecular dynamics, and identified the top 10 amino acids within CD91 or GP96 contributing the most to binding energy of CD91α-GP96 (Supplementary Fig. 21, Supplementary Table 1). The most binding-energy-contributing amino acids of GP96 were then mutated to Ala, and WT and mutant GP96 proteins were expressed, purified and characterized (Supplementary Fig. 22A-F). Experiments showed that these mutations within GP96 significantly affected its binding to CD91α (Supplementary Fig. 22G), thus verifying the binding interface between GP96 and CD91α. Based on the abovementioned experiments, a schematic diagram of the mode in which the RBD-GP96-Fusion vaccine is fixed on FDCs in GCs through binding to LRP1/CD91-α, in addition to FcRs and CR2 pathways, to enhance GC B cell activation, is presented as shown in Fig. 4R. By using the presented model that combines the results of Figs. 2D and 2E, we proposed that the RBD-GP96-Fusion strategy can enhance antigen stability, enter B cell follicles more effectively through sinuses, and target FDCs surface LRP1 with GP96 to accumulate more intact antigens for B cells, thereby causing a strong and long-lasting humoral immune response.

RBD-GP96-Fusion vaccines induce broad and long-lasting T cell responses by targeting DCs

Given the superiority of the interaction between $CD11c^{+}$ DCs and effector T cells with the GP96, we proceeded to subcluster T cells and identified 7 subsets based on the expression of canonical T cell markers (Supplementary Fig. 23A, B). As depicted in Figs. 5A and 5B, there was a notable increase in CD8 effector T cells bound to the RBD-GP96-Fusion protein compared to the RBD control. The enrichment of functional modules of DEGs in the various cell types indicates that the shared upregulation module is predominantly enriched in CD8 effector cells and focuses on leukocyte-mediated cytotoxicity, regulation of cell killing, and regulation of lymphocyte-mediated immunity (Supplementary Fig. 23C, D). Additionally, cell interactions between CD8 effector cells and cDCs are increased in RBD-GP96-Fusion protein-treated mice compared to RBD-control (Fig. 5C), as calculated by CellPhoneDB.

Then cellular immune response was examined in BALB/c and HLA-A2 transgenic mice after immunization (Fig. 5D). The RBD-GP96-Fusion immunization demonstrated higher levels of secreted TNF and IFN-γ by splenocytes, indicating a more prone Th1-type cellular immunity compared to the RBD with alum or GP96 group (Supplementary Fig. 24A). Further design of H-2-Kd and HLA-A2 epitopes was carried out[43–45] (Supplementary Table 2). After the third immunization, epitope-specific T cell immune responses were detected by ELISPOT (Supplementary Fig. 24B, C), and the conservation of these epitopes was predicted (Supplementary Fig. 24D). After screening out the highly efficient and conserved epitopes $S_{535\text{-}543}$ and $S_{424\text{-}432}$, intracellular cytokine staining (ICS) assays were conducted (Fig. 5E, F and Supplementary Fig. 25A). The above results showed that the RBD-GP96-Fusion vaccine could induce highly efficient cellular immune responses and had conservation against different virus strains. The results of the ICS assay and the frequencies of activation-induced marker $(AIM)^{+}$ $CD4^{+}$ and $CD8^{+}$T cells stimulated by $S_{535\text{-}543}$ or SARS-CoV-2 RBD peptide pool after the first immunization showed that the RBD-GP96-Fusion vaccine was significantly more effective than the RBD with alum or GP96 group (Supplementary Fig. 25B-D), suggesting that the RBD-GP96-Fusion vaccine may be able to establish cellular immune protection at an early stage.

Compared to RBD with alum or GP96 group, the proportion of $CD8^{+}$T cells secreting IFN-γ in the bronchoalveolar lavage fluid (BALF)

https://doi.org/10.1038/s41467-025-67092-x

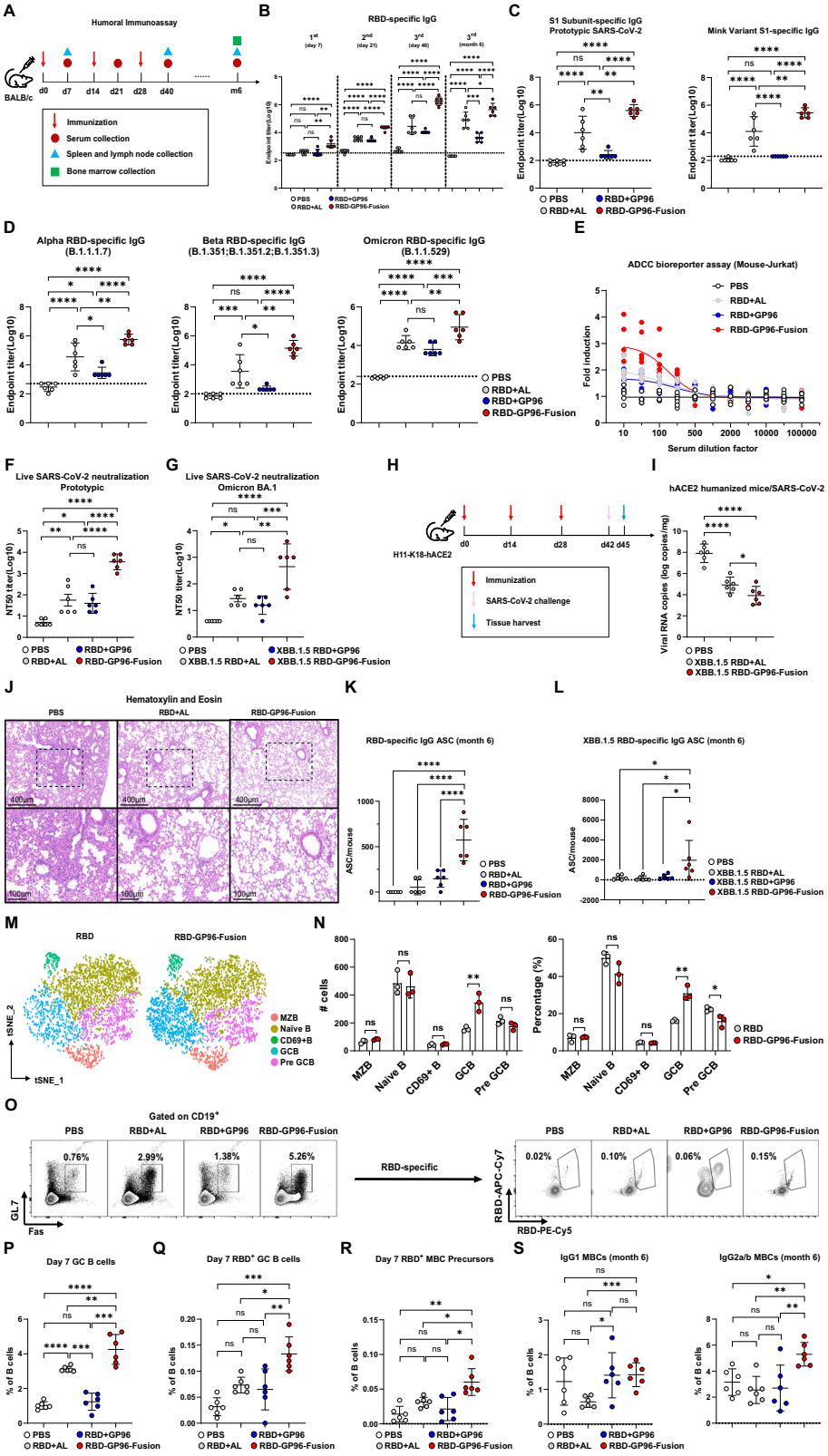

of the RBD-GP96-Fusion group after the third immunization sharply increased by 5.3-fold and 8.2-fold respectively (Fig. 5G, H, and Supplementary Fig. 26A), indicating that the vaccine could induce immunodominant epitope-specific $CD8^+$ T cells in the lung and airways[43,46]. Moreover, the expression of CD11a and CXCR6 in $CD8^+$T cells of the BALF was significantly enhanced (Fig. 5I, and Supplementary Fig. 26A, B), suggesting that the lung cellular immune response induced by RBD-GP96-Fusion vaccine might be driven by the corresponding chemokines for migration. And to further confirm that the drive originated from the lungs, we detected the lung tissue-resident memory T cells (Trm) and the corresponding integrins[43,46–48]. The results showed that RBD-GP96-Fusion group had significantly higher levels of $CD69^+CD103^+$ Trm of $CD4^+$ and $CD8^+$ T cells, as well as $\alpha4\beta7^+$ $CD4^+$ and $CD8^+$ T cells than control groups (Fig. 5J, K, and Supplementary

Fig. 3 | RBD-GP96-Fusion vaccines elicit robust IgG titers and strong antigen-specific GC B cell responses. Mice ($n = 6$ per group) were intramuscularly immunized with SARS-CoV-2 RBD vaccines (prototype or XBB.1.5 strain). **A** Schematic of RBD-GP96-Fusion induced humoral immunity. **B**–**G** Serum analyses at indicated time points. **B** RBD-specific IgG kinetics at day 7 post-immunization and 6 months after the 3rd dose. **C**, **D** S1-specific and cross-reactive RBD IgG against variants at day 7 post-3rd dose. **E** Serum ADCC activity. **F**, **G** Neutralization titers (NT50) against SARS-CoV-2 variants at day 7 post-3rd dose. **H** Immunization and challenge timeline. **I** Lung viral RNA by reverse transcription quantitative PCR (RT-qPCR) at day 3 post-infection. **J** H&E staining of lung tissues (scale bars: 400/100 μm). **K**, **L** Bone marrow RBD-specific and XBB.1.5-RBD-specific IgG$^+$ ASCs by ELISPOT at 6 months. **M**, **N** scRNA-seq of Cy5$^+$ cells in draining LNs: t-SNE visualization of B cell clusters (**M**) and absolute numbers/percentages of subsets (**N**). **O**–**R** Inguinal LN analysis at day 7 post-1st dose. **O** Flow cytometry of GC B cells and RBD-specific GC B cells. **P**, **Q** Frequencies of GC B cells and RBD-specific GC B cells. **R** Frequency of RBD-specific CCR6$^+$ MBC precursors in LZ. **S** IgG1$^+$ and IgG2a/2b$^+$ MBCs frequencies at 6 months. Data represent two independent experiments. Geometric mean ± SD shown; individual points represent mice. L.O.D. indicated (dotted line). Statistical analysis by one-way ANOVA with Bonferroni correction or unpaired two-tailed t-test. ns $p > 0.05$, $^*p \le 0.05$, $^{**}p \le 0.01$, $^{***}p \le 0.001$, $^{****}p \le 0.0001$.

Fig. 26C–I). However, the generation of RBD-specific IgA antibodies in the lungs could not be detected (Supplementary Fig. 26J).

To assess the long-term durability of cellular immunity maintenance, the spleen immune responses were examined 6 months after the third immunization. The peptide pool-stimulated AIM$^+$CD8$^+$T cell immune responsein the RBD-GP96-Fusion group remained significantly higher than the RBD with alum or GP96 group, whereas there was no significant difference in the AIM$^+$CD4$^+$T cell immunity[49] (Fig. 5L, and Supplementary Fig. 27). Among the main subsets of memory T cells, the stem cell-like memory T cells (Tscm) were significantly higher in the RBD-GP96-Fusion group (Supplementary Fig. 28), indicating that this cell subset is vital for maintaining long-term T cell immunity in this immune group[50]. After stimulation with the peptide pool, the corresponding antigen-specific activated effector memory T cells (Tem) and IFN-γ$^+$ CD8$^+$ Naïve T/Tem subtypes of memory T cells showed a significant increase (Supplementary Fig. 29). The cellular immune responses elicited by the SARS-CoV-2 XBB.1.5 RBD-GP96-Fusion vaccine constructed with the same strategy align with the trends observed in the above experiments (Supplementary Fig. 30).

The variation of the RBD signal intensity on the cell membrane surface after co-incubation of different antigens with bone marrow dendritic cells (BMDC) can indicate that RBD-GP96-Fusion can be enriched on the surface of BMDCs more quickly and in greater quantities (Fig. 5M, N). The immunofluorescence co-localization signals indicated that the antigen enrichment occurred through the binding of GP96 and CD91/LRP1 (Fig. 5O, P). Subsequently, the cross-presentation pathway after antigen endocytosis was analyzed via immunofluorescence co-localization signals, based on various treatments with endocytosis and autophagy-lysosomal inhibitor BAFA1 and proteasome inhibitor MG132. It was observed that more RBD was delivered to the ER under treatment with RBD-GP96-Fusion than RBD with Alum or GP96, and this process was strongly inhibited by BAFA1 and MG132 (Supplementary Fig. 31, 32). Similar results were observed on the Raw264.7 cell line (Supplementary Fig. 33). The results indicate that after endocytosis of the RBD-GP96-Fusion vaccine, it undergoes hydrolysis in the lysosome or proteasome, and RBD peptides are delivered to the ER for antigen presentation and T cell activation (Fig. 5Q, Supplementary Fig. 34 presents a schematic diagram).

We further conducted flow cytometry validation of major differential immune cell populations bound by the RBD-GP96-Fusion protein, following the process outlined in Supplementary Fig. 9A. The differences in absolute cell counts were consistent with the scRNA-seq conclusion (Supplementary Fig. 35), demonstrating the reliability of the above conclusion.

The HPV vaccine constructed by a fusion strategy induces potent antibodies, cellular immune responses, and virus clearance ability

To validate the universality of this GP96 fusion strategy, another vaccine was designed. For the modification of the HPV vaccine, the HPV-18 L1 is truncated at the C-terminal residue G535 and connected with GP96 protein N-terminal residue D22 to construct fusion protein[51]. The dimer structure was predicted using AlphaFold3, revealing that the L1 dimer primarily interacts with the NTD domain of GP96 (Fig. 6A, and Supplementary Fig. 36A, B). Additionally, the interaction sites between the L1-GP96-Fusion protein and the CD91α subunit align with those shown in Supplementary Fig. 20A, allowing for proper exposure of the L1 antigen (Supplementary Fig. 36C). The fusion protein was purified and analyzed by gel electrophoresis and TEM (Fig. 6B, C), revealing a stabilized compact conformation with both N- and C-terminal dimerization. The melting temperature (Tm) of L1-GP96-Fusion was significantly higher than that of HPV-L1 (Supplementary Fig. 37).

BALB/c mice were immunized three times, and their spleens and sera from various stages were collected for detection (Fig. 6D). Immunization was performed using 20 μg of L1 protein in combination with widely recognized HPV adjuvants (AS04C, AS04D, and MF59) as positive controls. The L1-GP96-Fusion induced a certain degree of improvement in antibody titer and quantification (Fig. 6E, F). There is no significant patternization difference in the types of antibody reactions and cross-immunity between L1-GP96-Fusion and classical adjuvants, except that L1-GP96-Fusion induced higher IgG2a production (Supplementary Fig. 38A–D), indicating enhanced Th1-type immune response. Corresponding to the antibody response, L1-GP96-Fusion immunization can also elicit a potent GCs response, causing a significant increase in the frequency of L1-specific GC B cells and MBC precursors (Fig. 6G–I). However, no significant differences in L1-specific IgG ASCs could be induced in the short term (Supplementary Fig. 38E).

The ICS assays showed a significantly increased trend in effector CD8$^+$ T cell response following L1-GP96-Fusion immunization, mainly reflected in the differences of CD8$^+$ IFN-γ$^+$ and Granzyme B$^+$ cytokines compared to immunization with L1 with AS04C/D, MF59 or GP96 adjuvant, suggesting a correlation with cytotoxic function (Supplementary Fig. 39, Fig. 6J). Additionally, the trends of AIM$^+$ T enhancement were consistent (Fig. 6K, L). Nevertheless, the results of ELISPOT and the examination of epitope conservation were rather disordered, and the monitoring of memory T cell responses still needs to be conducted over a longer period of time[52] (Supplementary Fig. 40, and Supplementary Table 3). We further employed HLA-A2 transgenic mice for immunization. The cell cytotoxicity assays using the HLA-A2 cell line MS751 expressing HPV type 18 virus demonstrated that the killing ability of the L1-GP96-Fusion immunization against virus-infected cells was much stronger than that of the classical MF59 adjuvant (Fig. 6M, N, and Supplementary Fig. 41A, B). And this cytotoxic effect is mainly mediated by CD8$^+$ T cells (Supplementary Fig. 41C, D). Considering the correlation between the frequency of CD8$^+$IFN-γ$^+$ T cells and the observed killing (Fig. 6O), it can be concluded that the T cell immune response primarily contributed to this effect.

We further used HPV E7 antigen to evaluate superior T cell effector responses by GP96-fusion approach, as E6 and E7 were more closely related to the immunotherapy of HPV-driven cancers[53,54]. We constructed the E7-GP96-Fusion protein (Supplementary Fig. 42A, B). The effector T cell immune responses were detected by the ICS assays with cocktail stimulation 14 days after the third immunization (Supplementary Fig. 42C). E7-GP96-Fusion can induce highly potent effector T cell immune responses, mainly concentrated on the key cytotoxic cytokines CD8$^+$ IFN-γ$^+$, Granzyme B$^+$, and Perforin$^+$ (Fig. 7A–D), which are stronger than those induced by L1-GP96-Fusion. The subcutaneous HeLa xenograft model was used to challenge HPV$^+$

https://doi.org/10.1038/s41467-025-67092-x

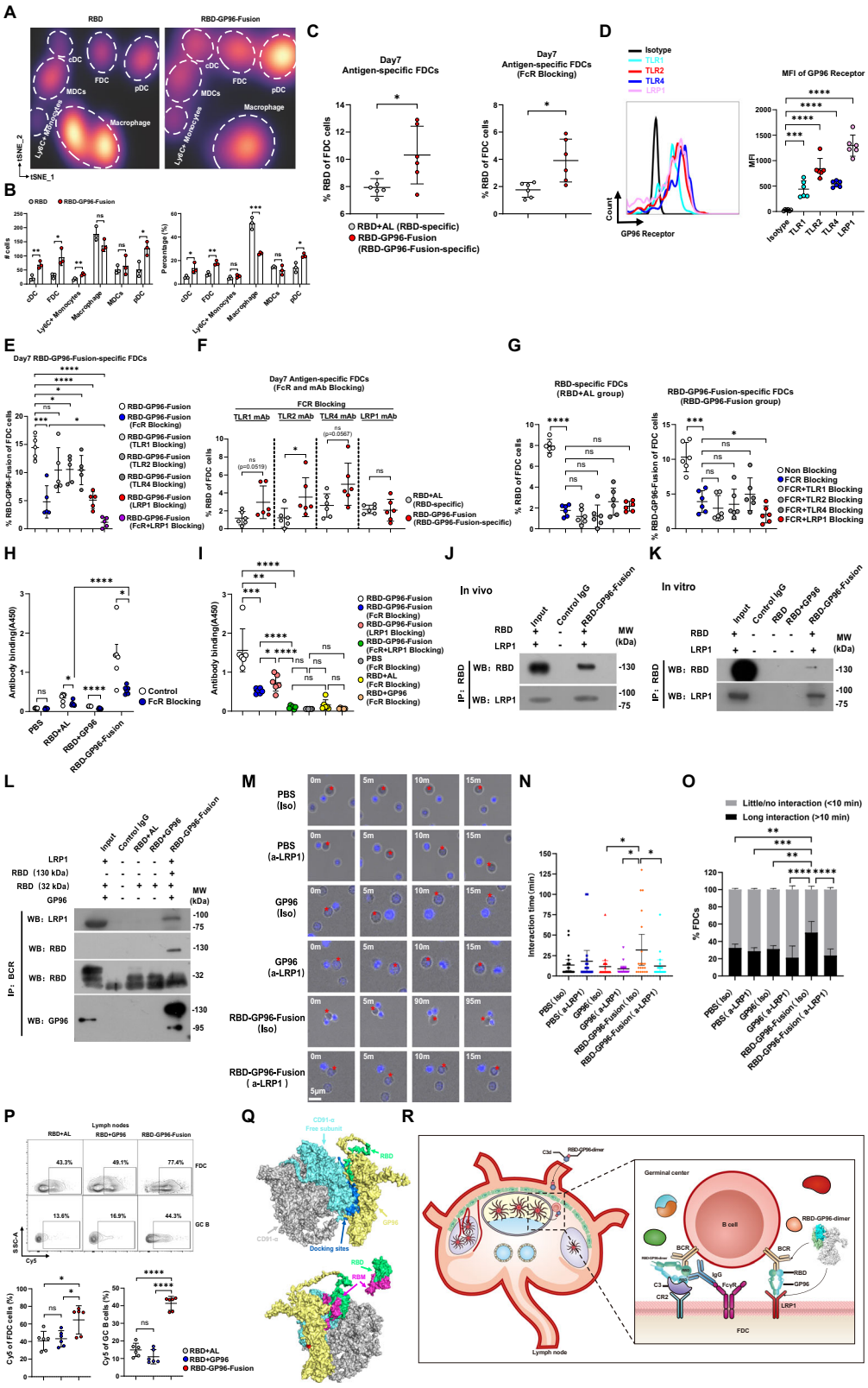

tumors. The effect of E7-GP96-Fusion immunization on tumor growth was investigated by tail vein reinfusion of CD8⁺ T cells from HLA-A2 transgenic mice immunized with E7-GP96-Fusion or E7 with MF59 or GP96 adjuvant (Supplementary Fig. 42C, D, Fig. 7E). As a result, the smallest tumor volume (Fig. 7F, G), the lowest tumor weight (Fig. 7H), the most CD8⁺ T cell infiltration were observed in the E7-GP96-Fusion immunization group (Fig. 7I, J).

Discussion

In this study, we present a novel vaccine strategy that employs the fusion of the RBD from SARS-CoV-2 or the L1 and E7 proteins from HPV with GP96 to enhance the immunogenicity and stability of these antigens. The GP96 protein exhibits a unique structural composition that enhances its utility as a potent adjuvant in vaccine formulations. This design leverages GP96's inherent C-terminal dimerization

Fig. 4 | RBD-GP96-Fusion vaccines generate alternative antigen retention mechanisms in GCs via GP96 and FDCs. Mice were immunized i.m. with SARS-CoV-2 RBD vaccines. Inguinal LNs were collected 7 days post-1st immunization. **A** Galaxy plots of monocyte subsets. **B** Absolute numbers and percentages of each cell type ($n = 3$). **C** Frequency of FDCs and RBD$^+$/RBD-GP96-Fusion$^+$ FDC cells ($n = 6$). **D** Flow cytometry analysis of LRP1 and TLRs expression on FDCs (isotype: PE Rat IgG2a, κ). **E**–**G** Frequency of RBD$^+$/RBD-GP96-Fusion$^+$ FDCs after blocking with indicated mAbs. **H**, **I** RBD-specific Ab titers at day 14 post-immunization with FcR/LRP1 blocking. **J**–**L** IP and Western blot of LRP1-GP96-antigen-BCR complex in FDCs from immunized (**J**, **L**) or non-immunized (**K**) mice. (**J**) FDC cell sorting was subjected to IP with RBD mAb and Western blotting using RBD and LRP1 mAbs. **K** FDC cell sorting was incubated with the recombinant RBD protein, RBD protein with GP96 and RBD-GP96-Fusion protein. The incubated FDCs were subjected to IP with RBD mAb and Western blotting by LRP1 mAb. **L** Lymph node cells were directly subjected to IP by Protein A/G agarose and Western blotting with LRP1, RBD and GP96 mAbs, respectively. **M**–**O** GP96-stimulated FDCs enhance GC B cell interactions in LRP1-dependent manner. **M** FDCs from inguinal LNs were treated with GP96, RBD-GP96-Fusion, and with or without α-LRP1 or isotype control antibody. Hoechst-labeled GC B cells were then added at a 1:1 ratio. Time-lapse images were captured every 5 minutes for 1–2 h to analyze cell interactions and motility. (N) B cell tracking and interaction time quantification ($n = 20$). **O** Percentage of B cells with long (>10 min) vs short (0–10 min) interactions ($n = 20$). **P** Frequency of Cy5$^+$ FDC or Cy5$^+$ GCB cells. **Q** ZDOCK model of RBD-GP96-Fusion bound to CD91-α receptor. **R** Schematic of antigen acquisition by FDCs. Data are from $n = 6$ mice/group unless specified, representative of two experiments. Geometric mean ± SD shown; individual points represent mice. Statistics: one-way ANOVA with Bonferroni correction or unpaired two-tailed t-test. ns $p > 0.05$, $^*p \le 0.05$, $^{**}p \le 0.01$, $^{***}p \le 0.001$, $^{****}p \le 0.0001$.

capabilities, allowing the N-terminal region to serve as a flexible binding site that supports the stable association of a wide range of antigens with a molecular weight of tens of kDa while preserving critical epitopes such as RBMs. This structural configuration also promotes the formation of nanoscale particles (10-14 nm) (Fig. 1H), which protect the antigen from proteolytic degradation and enhance its immunogenic profile. Importantly, fusion of antigens at the N-terminal minimizes the conformational instability observed with larger antigens and reduces the randomness of antigen binding (see Supplementary Fig. 2A, Fig. 1D and Fig. 2), thus addressing limitations associated with traditional antigen-adjuvant formulations. These findings underscore the structural advantages of GP96 and highlight its potential to produce robust and durable immune responses.

The N-terminal fusion strategy effectively increases RBD antigen stability, creates a depot effect, and does not decrease its antiviral immunogenicity. This strategy might enable more intact antigens to pass through the high protease-active sinuses of lymph nodes, and effectively generate a strong T and B cell immunity. Mechanically, the fusion protein binds to FDC and engages with receptor LRP1, supporting robust GCB responses[35,37,38,55]. This prolonged antigen retention mediated by GP96 within GCs stimulates high-affinity and long-lasting antibody production, addressing limitations in the durability and cross-protection of traditional vaccines. The interaction between GP96 and FDCs ensures sustained antigen exposure in GCs, thereby promoting both immediate antibody responses and the formation of memory B cells (Supplementary Fig. 43). In light of the key role of GCs in the generation of long-lived plasma cells and high-quality persistent Ab responses, our GP96 fusion approach offers a versatile platform for enhancing immune responses against a range of viral pathogens with low immunogenicity.

Administration of antigen-GP96 fusion vaccine was well tolerate in mice, with no effect on body weight or other obvious toxicity. RBD-GP96-Fusion only induced modest inflammatory response after repeated immunization (Supplementary Fig. 7F), which is far below the threshold level of triggering cytokine storms[11]. Similar results were observed in other studies using GP96 as adjuvant[56,57]. Mechanistically, unlike the specific ligands of TLRs (such as LPS for TLR4), the binding between GP96 as a chaperon and its client TLRs may occur at a dynamic and transient level. The duration and intensity of this interaction are relatively weak, and may not trigger excessive and prolonged activation of TLRs and the downstream pathways.

The GP96-based adjuvant strategy offers distinct benefits compared to conventional and common adjuvants such as alum, MF59, and AS04, which primarily act by nonspecific immune stimulation. Antigen-fused GP96 directly targets receptor LRP1/CD91, which enhances both humoral and cellular immunity by promoting antigen retention, precise antigen presentation, and enabling sustained B cell stimulation and effective cross-presentation to CD8$^+$ T cells. Indeed, the GP96 fusion strategy has demonstrated a significant superiority over the aforementioned adjuvants in inducing stronger, broader, and longer-lasting antigen-specific antibody and T cell immunity (Fig. 3 and Fig. 5). Importantly, the conserved nature of GP96 across species minimizes the risk of autoimmune responses (see Supplementary Fig. 8D), making it a safer option for clinical translation. To further strengthen the translational capacity of this platform in the subsequent research, we conducted a more in-depth analysis of the binding interface between CD91 and GP96 (Supplementary Figs. 21, 22). This could allow to anticipate interference or competition in future vaccine designs. Finally, GP96's structural simplicity facilitates efficient production and scalability[58], presenting a strong foundation for its integration into next-generation vaccine platforms.

RBD-GP96-Fusion was found to induce CD8$^+$T cell response in BALF (see Fig. 5 and Supplementary Fig. 26). Eva Fisher et al. have shown that gp96-Ig immunization increases the frequency of CD11c^{high} MHC II^{high} CD103$^+$ cells at the immunization site. Together with the results of current study, we propose that RBD-GP96-Fusion immunization may increase CD103$^+$ DCs frequency at the site of immunization, promoting the differentiation of Trm CD8$^+$ T cells, and thus facilitating their migration to peripheral epithelial tissues including the lungs. Additionally, RBD-GP96-Fusion could enhance CXCR6 expression of CD8$^+$ T cells that may control T cell localization in the lungs. These mediate the generation of T cell immunity in the lungs. Nevertheless, our study did not observe significant IgA production in the lungs, an essential component of mucosal immunity for respiratory pathogens. This absence may be attributable to the subcutaneous administration route; thus, future studies should explore alternative delivery methods, such as intranasal administration, to stimulate mucosal immune responses.

Although the total number of GC-localized Tfh cells remained unchanged across experimental groups, we observed significant functional polarization, characterized by divergent secretion of the instructive cytokines IL-4 and IFN-γ (Supplementary Fig. 16D-F) in RBD-GP96-Fusion group. This qualitative shift rather than quantitative expansion may provide a mechanistic basis for the differential class-switching patterns in GC B cells. Elevated IL-4$^+$ Tfh activity promotes IgG1 switching[59], correlating with enhanced anti-RBD IgG1 titers by RBD-GP96-Fusion immunization. Increased IFN-γ$^+$ Tfh drives T-bet-mediated IgG2 switching[60,61], aligning with the surge in IgG2a antibody observed in RBD-GP96-Fusion group. It is likely that alterations in Tfh cytokine profiles by RBD-GP96-Fusion can reshape GC outcomes, as IL-4 and IFN-γ serve as direct molecular switches for antibody subclass commitment. Additionally, while GP96 has demonstrated efficacy in generating memory T and B cells, further elucidation of the molecular mechanisms underlying this process is warranted to optimize long-term immunogenicity. An important area for future investigation lies in balancing GP96's dual roles in immune activation and regulation, which may enhance its safety profile and efficacy across various clinical contexts.

RBD-GP96-Fusion was shown to equally bind to SARS-CoV-2 receptor hACE2 and efficiently induce NAbs mice, partly validating

https://doi.org/10.1038/s41467-025-67092-x

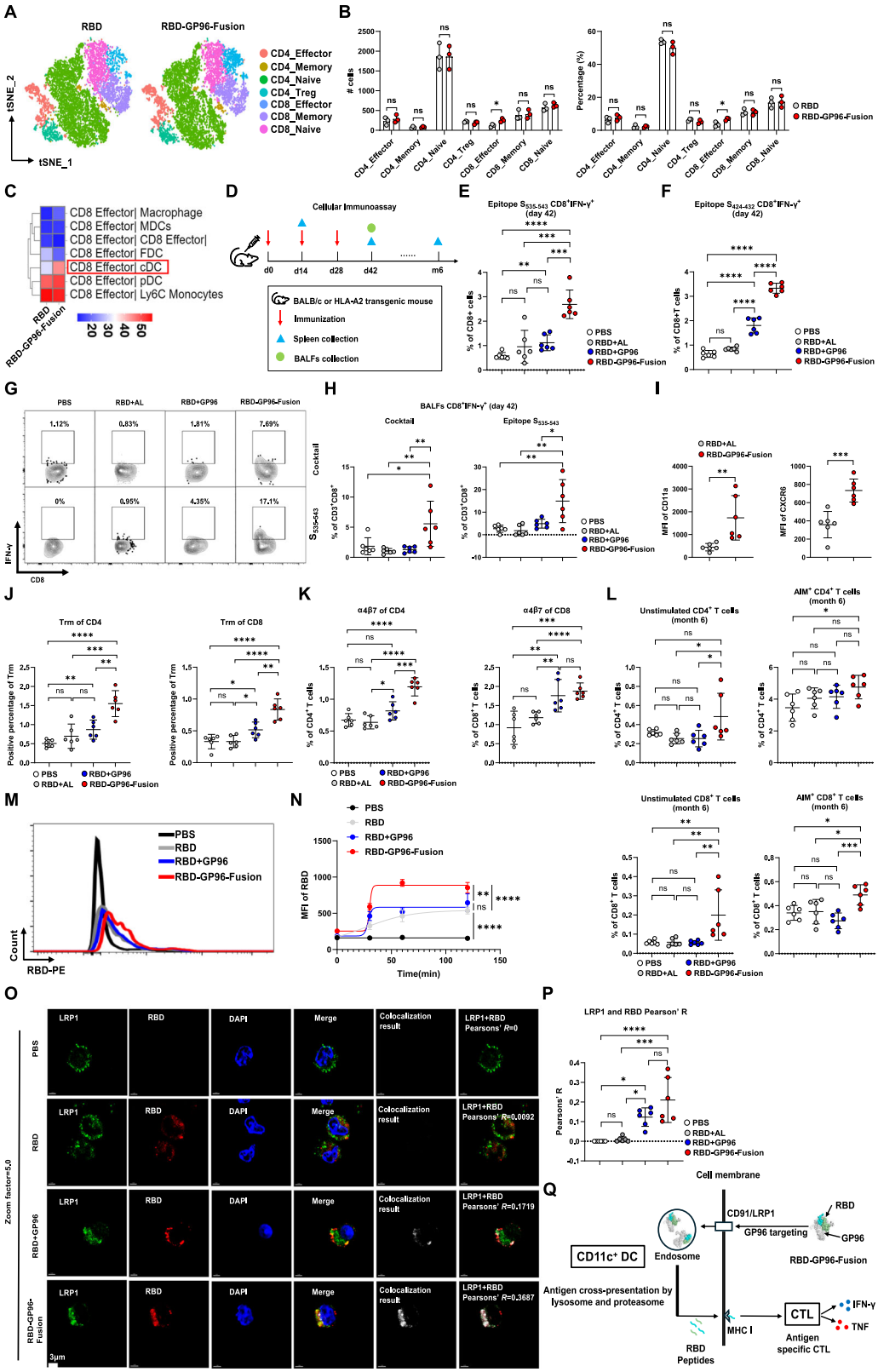

RBD antigen exposure when fused with GP96. Nevertheless, experimentally solved binding interactions (cryo-electron microscopy and X-ray crystallography) between viral antigens and GP96 will be needed to avoid potential biases of AlphaFold3 folding metrics. It should be noted that to avoid misfolded protein or lack of dimer when designing for different antigens, unnecessary flexible regions should be removed to the greatest extent possible, and large-scale protein structure prediction analysis should be combined. Structure validation and quality control of GP96 fusion proteins are needed to ensure efficient engagement with B cells. In addition, the structural issues caused by post-translational modifications (such as glycosylation) of proteins can also be optimized through the improvement of expression systems, for instance, the 293 F expression system. Protease inhibitors can be incorporated to safeguard against protein degradation. Finally,

Fig. 5 | RBD-GP96-Fusion vaccines induce broad and long-lasting T cell responses by enhancing the targeting of DC cells. BALB/c or HLA-A2 transgenic mice were immunized with indicated vaccines. **A** t-SNE plot of T cell subpopulations. **B** Absolute numbers and percentages of each cell type ($n = 3$). **C** Cell-cell contact analysis between $CD8^+$ effector and DC cells by CellPhoneDB. **D** Schematic of cellular immune responses induced by RBD-GP96-Fusion. **E**, **F** Spleen and **G**–**K** BALF collected at day 14 post-3rd immunization; **L** Spleen at 6 months post-3rd immunization. **E**, **F** ICS assay of splenic $CD8^+$ T cells producing IFN-γ upon epitope stimulation. **G**–**I** An ICS assay was performed to assess the ability of BALFs to secrete IFN-γ following stimulation with cocktail or dominant $CD8^+$ epitope $S_{535\text{-}543}$. **G** Representative flow plots of BALF $CD8^+IFN\text{-}\gamma^+$ cells. **H** Frequencies of epitope-specific $CD8^+IFN\text{-}\gamma^+$ cells in BALF. **I** CD11a and CXCR6 expression on BALF $CD8^+IFN\text{-}\gamma^+$ cells. **J**, **K** Frequencies of Trm (**J**) and $\alpha4\beta7^+$ (**K**) cells in BALF $CD4^+/CD8^+$ T cells. **L** AIM^+ ($CD137^+OX40^+$) $CD4^+$ and AIM^+ ($CD137^+CD69^+$) $CD8^+$ T cells in splenocytes after RBD peptide stimulation. **M** MFI of RBD-TRITC on BMDCs after incubation with indicated proteins. **N** The kinetics of MFI as (**M**) over time. **O** Confocal microscopy of BMDCs showing nucleus (DAPI), LRP1 (FITC), and RBD (TRITC). **P** Percentage of ROI with LRP1-RBD colocalization. **Q** Schematic of RBD-GP96-Fusion mediated antigen cross-presentation via CD91/LRP1. Data from $n = 6$ mice/group (E-L) or $n = 6$ fields (**M**–**P**), representative of two experiments. Geometric mean ± SD shown. Statistics by one-way ANOVA with Bonferroni correction or unpaired two-tailed t-test. ns $p > 0.05$, $^*p \le 0.05$, $^{**}p \le 0.01$, $^{***}p \le 0.001$, $^{****}p \le 0.0001$.

expanding the GP96 fusion strategy to additional antigens with poor intrinsic immunogenicity or high mutation rates, such as influenza or enteroviruses, would extend the applicability of this adjuvant platform, addressing a critical need in vaccine development for rapidly evolving pathogens. Continued exploration of these areas will be essential to fully realize the clinical potential of GP96 as a versatile and powerful adjuvant in vaccine design.

Methods

All methods in this study were performed in compliance with relevant ethical regulations under a protocol approved by the Institutional Ethics Committee of the Institute of Microbiology, Chinese Academy of Sciences.

Mice

Specific pathogen-free (SPF) 6-8-week-old female BALB/c (Stock No. 211), BALB/c nude (Stock No. 401) were purchased from Beijing Vital River Laboratory Animal Technology Co., Ltd. (Beijing, China). HLA-A2.1/Kb (HLA-A2) transgenic mice were maintained in the laboratory[62]. Specific pathogen-free (SPF) 6-8-week-old female H11-K18-hACE2 transgenic mice were purchased from GemPharmatech Co., Ltd. (Jiangsu, China) (Stock No. T037657). All mice used in this study are in good health and have not been involved in any other experimental procedures. They were housed under SPF conditions in the laboratory animal facilities at Institute of Microbiology, Chinese Academy of Science (IMCAS) and Institute of Laboratory Animal Sciences, Peking Union Medical College. Mice were housed with six companions per cage. All animals were given unrestricted access to water and a standard chow diet and provided with a 12-h light and dark cycle, with a temperature range of 20–25 °C and humidity levels between 40% and 70%. Experimental and control animals were housed separately throughout the study. Euthanasia was performed by the Carbon dioxide (CO2) inhalation or cervical dislocation method. Animal studies were carried out in accordance with the guidelines set forth by the Institute of Microbiology, Chinese Academy of Sciences of Research Ethics Committee under the approved protocol numbers APIMCAS2022128.

Cell culture

Hu94, H7-3, ME180, MS751, SiHa, Hela and RAW264.7 cell lines were obtained from ATCC (Manassas, VA, USA). The Jurkat-mFcγRIII-NFAT-Luc reporter cells (Promega) were donated by the laboratory of Yi Shi (Institute of Microbiology, CAS). The cell lines used in the experiments were all cultured in Roswell Park Memorial Institute 1640 (Gibco BRL, Paisley, UK) with 10% FBS. All culture media contained 100 U/mL penicillin and 100 μg/mL streptomycin. Sf9 (Invitrogen) insect cells were cultured in SIM SF Expression Medium (SinoBiological) at 28 °C.

Protein structure prediction and modeling

AlphaFold3 was used to predict the structure of the monomer of GP96, RBD-GP96-Fusion, LI-GP96-Fusion, and CD91-α. The amino acid sequences of human GP96, SARS-CoV-2 RBD, HPV18 L1, and CD91-α were downloaded from NCBI. And the dimer structures were predicted using the AlphaFold2-Multimer 2.2.4. The ranked_0 structure files of GP96-dimer and RBD-GP96-Fusion dimer were selected for subsequent molecule dynamics analysis. ZDOCK version 3.0.2 was used to predict the complex model of the receptor and ligand via rigid docking. The final results were visualized and analyzed using PyMol 2.5.

Molecule dynamics

The GP96 protein dimer, RBD-GP96-Fusion dimer and CD91-GP96 built using the AlphaFold3 method were simulated separately using full-atom molecular dynamics simulations, which were performed using the AMBER 18 software. Before the simulations, the proteins were described using the ff14SB protein force field. Each system was equipped with hydrogen atoms using the LEaP module. A truncated octahedral TIP3P solvent box was added at a distance of 10 Å from the system. Na^+/Cl^- ions were added to balance the system charge, and the topology and parameter files for the simulation were output. Before the simulations, the system was optimized for energy, including 2500 steps of steepest descent and 2500 steps of conjugate gradient. After the system energy optimization was completed, the system was heated up to 298.15 K at a constant volume and constant heating rate over 200 ps, so that the system temperature was slowly raised from 0 K. Under the condition of maintaining the system temperature at 298.15 K, a 500 ps NVT (constant temperature and constant volume) simulation was conducted to further distribute the solvent molecules evenly in the solvent box. A 500 ps NPT equilibrium simulation was conducted on the entire system, followed by a 100 ns simulation of the two composite systems under NPT periodic boundary conditions. During the simulations, the non-bonded cutoff distance was set to 10 Å. The Particle mesh Ewald (PME) method was used to calculate the long-range electrostatic interactions, while the SHAKE method was employed to limit the hydrogen bond length. The Langevin algorithm was utilized for temperature control, with a collision frequency γ set to 2 ps^{-1}. The system pressure was set to 1 atm, the integration step was 2 fs, and the trajectories were saved every 10 ps for subsequent analysis.

Protein expression and purification

The baculovirus expressed recombinant SARS-CoV-2 RBD, GP96, RBD-GP96-Fusion, HPV18 L1, HPV18 L1-GP96-Fusion, CD91-α, GP96-Mutant, HPV18 E7 and HPV18 E7-GP96-Fusion proteins were expressed with the Bac-to-Bac baculovirus expression system (Invitrogen). The coding sequence for SARS-CoV-2 RBD (S protein residues 319–545, GenBank: PP084047.1), GP96 (residues 22 – 799, GenBank: NM_003299) and HPV18 L1 (residues 81-535, GenBank: MH057745.1) were codon-optimized and cloned into the baculovirus transfer vector pFastBac1 (Invitrogen). For each construct, gp67 signal peptide sequence was added to the protein N terminus for protein secretion, and a hexa-His tag was added to the C terminus to facilitate further purification processes.

Transfection and virus amplification were conducted with Sf9 cells, and the recombinant proteins were produced in Sf9 cells (Invitrogen) for 72 h. The cell supernatants were then collected and soluble proteins were recovered through a 5 mL HisTrap HP column (GE Healthcare). After removal of most of the impurities, the recovered

https://doi.org/10.1038/s41467-025-67092-x

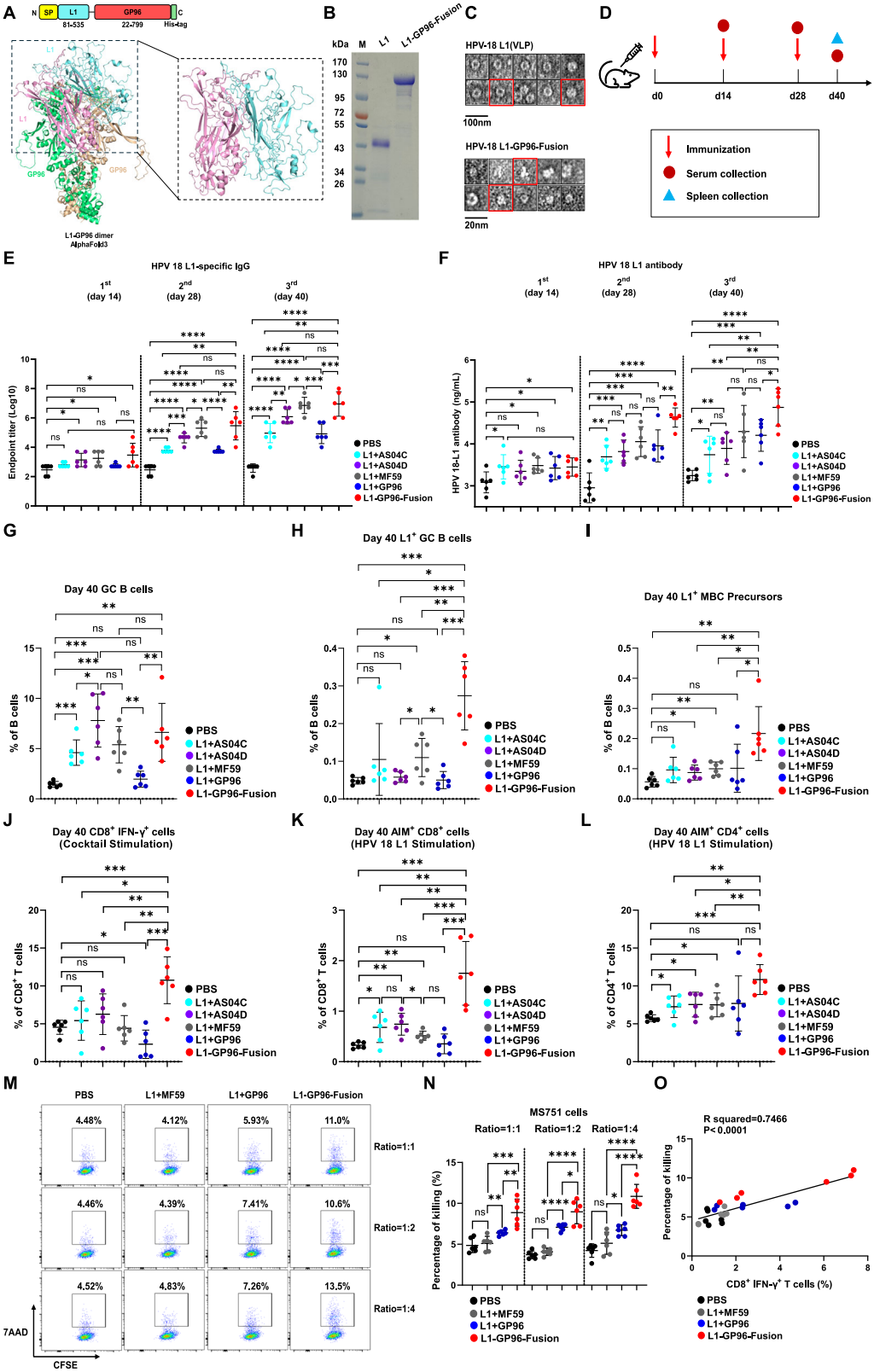

proteins were further purified by gel-filtration chromatography using a HiLoad 16/600 Superdex 200 pg column (GE Healthcare) with a running buffer of 20 mM Tris-HCl and 150 mM NaCl (pH 8.0).

Analytical ultracentrifugation

Sedimentation velocity experiments were carried out on two samples (SARS-CoV-2 RBD-GP96-Fusion and HPV18 L1-GP96-Fusion) using the Proteome Lab XL-I analytical ultracentrifuge (Beckman Colter, Brea, CA). A volume of 380 µL of protein sample (A280 = 0.6 − 0.8) and 400 µL of matching buffer (20 mM Tris, 150 mM NaCl, pH8.0) were injected into appropriate channels of 12 mm double sector aluminum epoxy cells with sapphire windows. Solutions were centrifuged at 39,000 rpm at 20 °C in an An-60Ti rotor for 8 h. Scans were collected at 280 nm, with 3 minutes interval between each scan. Data were

Fig. 6 | Design and assessment of L1-GP96-Fusion as a vaccine against HPV by fusion strategy. Groups of 6- to 8-week-old female BALB/c or HLA-A2 transgenic mice ($n = 6$) were i.m. immunized with HPV-18 L1 vaccines adjuvanted with AS04C, AS04D, MF59, or GP96, and L1-GP96-Fusion vaccine. Naïve mice were also included. **A** A schematic diagram of HPV-18 L1-GP96-Fusion (monomer). The structure of the L1-GP96-Fusion dimer was predicted based on AlphaFold3. **B** Reduced SDS-PAGE migration profiles of the pooled samples are shown. **C** Transmission electron microscopy of HPV-18 L1 and L1-GP96-Fusion protein. The red frames represent typical TEM structures. **D** Immunization schedule of HPV-18 L1 or L1-GP96-Fusion vaccines. **E**, **F** Serum was collected at various time points for analysis by ELISA. Kinetics of L1-specific IgG titers are shown (7 days after immunization). **G**–**I** Frequency of GC B cells (**G**), L1-specific GC B cells (**H**) or L1-specific MBC precursors (**I**) at 12 days post 3rd immunization by flow cytometry. **J** Frequencies of $CD8^+IFN\text{-}\gamma^+$ cells following stimulation with cocktail in the spleen at 12 days post-3rd immunization are shown by flow cytometry. **K**–**L** The frequency of AIM^+ ($CD137^+OX40^+$) cells (**K**) among $CD4^+$ T cells and the frequency of AIM^+ ($CD137^+CD69^+$) cells (L) among $CD8^+$ T cells were analyzed (12 days post 3rd immunization) by flow cytometry. **M** Representative analysis of various vaccines immune group-mediated killing of MS751 cell line (infected with HPV-18) by flow cytometry. **N** The frequency of killing percentage at different cell ratios was analyzed as (**M**). **O** Spearman correlation of L1-specific $CD8^+IFN\text{-}\gamma^+$ cells frequency and killing percentage. In (**E**–**O**), $n = 6$ mice per group were analyzed. The data are representative of two independent experiments with similar results. The geometric mean ± geometric SD is shown, and each data point represents an individual mouse or field. One-way ANOVA with Bonferroni correction or unpaired two-tailed t tests were conducted according to the distribution of the data. ns p å 0.05, $^*p \le 0.05$, $^{**}p \le 0.01$, $^{***}p \le 0.001$, $^{****}p \le 0.0001$.

analyzed using the continuous sedimentation coefficient distribution c(s) model in SEDFIT software.

Transmission electron microscopy structural analysis

Heavy metal salts (such as uranyl formate, uranyl acetate dihydrate, and phosphotungstic acid) were utilized as staining agents for negative staining of proteins for sample preparation. Subsequently, a transmission electron microscope JEM-1400 was employed for the preliminary structural analysis of the samples. Through concentration gradient screening, the optimal resolution concentrations of GP96, RBD-GP96-Fusion, L1, and L1-GP96-Fusion were 2.5 μg/mL, 5 μg/mL, 100 μg/mL, and 5 μg/mL, respectively.

Surface Plasmon Resonance

The Surface Plasmon Resonance (SPR) assays were carried out at 25 °C using a BIAcore 3000 machine with CM5 chips (GE Healthcare). All proteins for SPR assays were exchanged to PBST buffer (10 mM Na2HPO4; 2 mM KH2PO4, pH 7.4; 137 mM NaCl; 2.7 mM KCl; 0.005% Tween 20). The RBD-monomer and RBD-GP96-Fusion of SARS-CoV-2 were immobilized onto CM5 chips in pairs, respectively, at ~1000 response units (RUs). Gradient concentrations of hACE2 (ranging from 3.125 nM to 800 nM for SARS-CoV-2 RBD and RBD-GP96-Fusion) were then flowed over the chip surface at 30 μL/min, and the real-time response was recorded. After each cycle, the sensor surface was regenerated using 7 μL of 10 mM NaOH. The binding kinetics were analyzed using 1:1 binding model with the software BIAevaluation Version 4.1 (GE Healthcare).

Protein thermal stability analysis by nanoDSF

Thermal stability analysis was performed using a PR.NT.48 nanoDSF instrument (NanoTemper Technologies). Purified SARS-CoV-2 RBD, GP96, RBD-GP96-Fusion, HPV-L1 and L1-GP96-Fusion proteins (0.5–1.0 mg/mL in PBS, pH 7.4) were loaded into silica capillaries (10 μL/sample). Samples were heated from 20 °C to 95 °C at 1 °C/min. Melting temperature (Tm) was determined by monitoring the intrinsic tryptophan/tyrosine fluorescence ratio (F350/F330) during unfolding. Aggregation onset temperature (Tagg) was simultaneously measured via back-reflected light scattering at 650 nm. Data were analyzed using PR.Control software (v3.4.0), with Tm and Tagg defined as the inflection points of their respective derivative curves. Experiments were performed in triplicate and results were reported as mean ± SD.

Protein binding assay

The binding of gp96 was quantified by ELISA assay. Briefly, Nunc Maxisorp flat-bottom 96-well plates (Invitrogen, 44-2404-21) were coated with the receptor proteins (10 μg/ml). After blocking with 5% skim milk at 37 °C, serial concentrations of purified gp96 ranging from 0 to 100 μg/ml were added to each well in 100 μl of binding buffer (20 mM HEPES (pH 7.2), 20 mM NaCl, 2 mMMgCl2 and 100 mM KCl) to allow binding for 1.5 h. Afterwards, the plates were incubated with anti-gp96 antibody and the HRP-conjugated secondary antibody. The substrate TMB (3, 3′, 5, 5′-Tetramethylbenzidine) was used for detection. The reaction was measured at 450 nm.

In vivo imaging study

RBD, GP96, or RBD-GP96-Fusion proteins were independently conjugated with R-Cy5 using Lightning-Link R-Cy5 (Abcam, ab188288) kits, following the manufacturer's instructions. Subcutaneous immunization of mice on the back was conducted with labeled proteins of equal fluorescence intensity and the same molar quantity, and images were recorded with the IVIS Imaging System (Xenogen) 15 min after the injection. Subsequently, fluorescence imaging graphs were captured at various time points in accordance with different studies. The bioluminescence images were analyzed using Living Image software (Xenogen).

Immunization

RBD was diluted in phosphate buffered saline (PBS, Corning, 21-031-CV) and combined in a 1:1 ratio with aluminum hydroxide (Bioss, C07-01013) or with 15 μg recombinant GP96 adjuvant in each dose. RBD-GP96-Fusion was diluted in PBS prior to inoculation. The mixture of HPV18 L1 protein and multiple adjuvants is carried out in the same manner as described above. Each mouse was immunized with 5 μg of RBD protein and 20 μg of RBD-GP96-Fusion protein (of equivalent molar amounts). The immunization strategy for L1 protein was the same as above. Vaccines were injected into the gastrocnemius muscle using a 0.5 mL 28 G x 1/2" insulin syringe (BD Biosciences, 329461). For booster immunizations, the same dose of the respective vaccine was injected into the same site as the primary immunization.

Sample collection and processing

After immunization, mice were anesthetized with isoflurane and blood was collected from the orbital sinus using capillary tubes without anticoagulant for sera separation at the time of blood collection. Inguinal and popliteal LNs, spleens, and both tibias and femurs were harvested and placed in cold complete Dulbecco's Modified Eagle's Medium [(DMEM, Corning, T10014CV) containing 10% heat-inactivated Fetal Bovine Serum (FBS, Corning, 35-015), 1% Glutamax (Gibco, 35050-061) and 1% Penicillin/Streptomycin (Gibco, 5070063)]. All organs were kept on ice and immediately processed after collection.

LNs and spleen processing: Organs were homogenized with a syringe plunger and filtered through a 40 mm cell strainer on ice. Red blood cells (RBCs) of spleens were lysed using ACK lysing buffer (Lonza, 10-548E) for 5-8 minutes on ice, and the reaction was stopped with cold PBS.

Bone Marrow (BM) processing: BM was flushed from both femurs and tibias from each mouse using a 1 mL 25 G x 5/8" syringe (BD Biosciences, 30962). RBCs were lysed as described above.

Cells from all tissues were resuspended in ice cold complete DMEM and immediately used for counting, culture, or staining.

https://doi.org/10.1038/s41467-025-67092-x

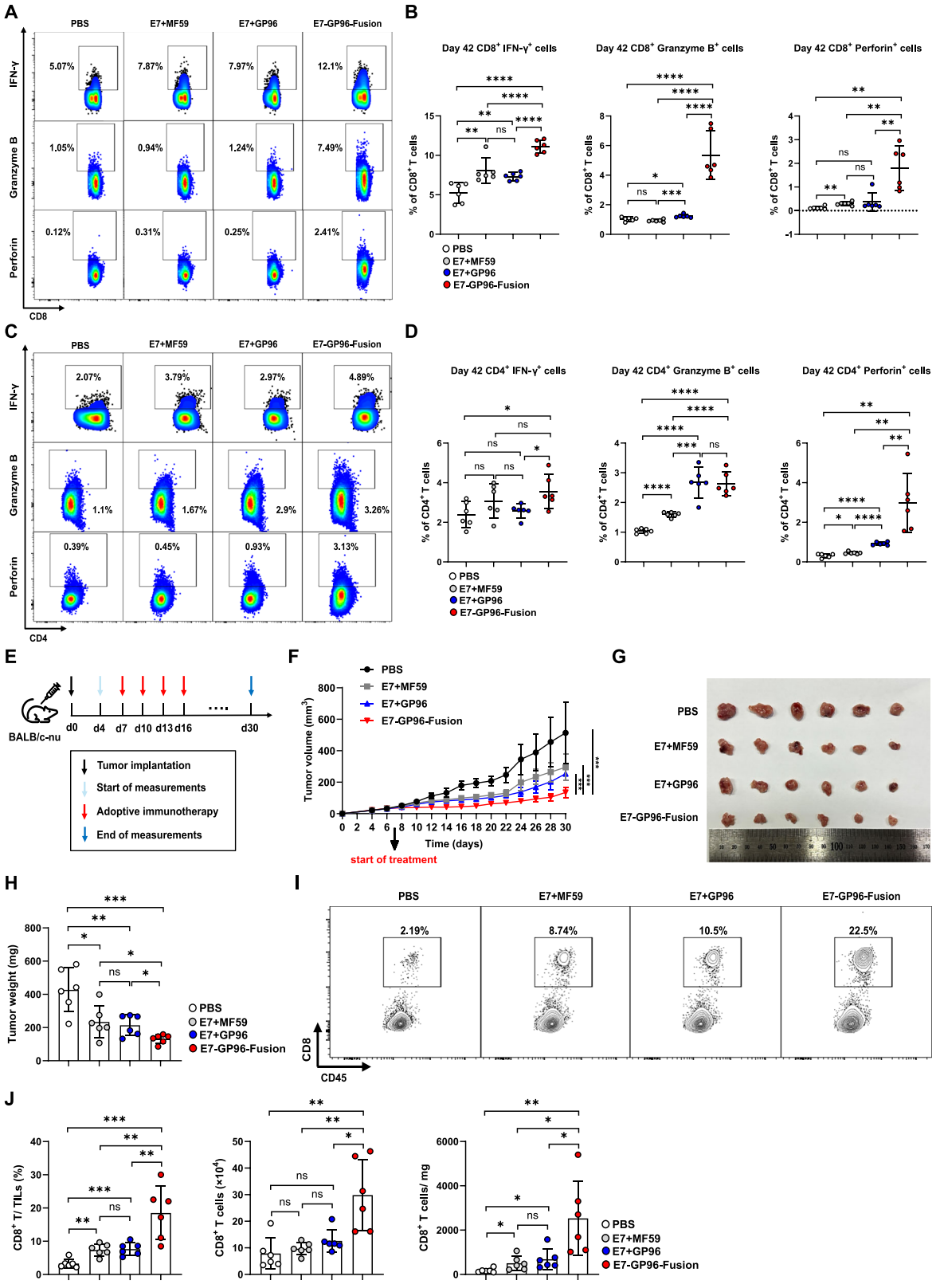

Following collection, blood was centrifuged at 14,000 g (maximum speed) for 30 minutes, 4 °C. Serum was recovered and stored at −20 °C for neutralization assays and ELISAs.

ELISA

Nunc Maxisorp flat-bottom 96 well plates (Invitrogen, 44-2404-21) were coated with 2 µg/mL SARS-CoV-2 RBD protein or HPV18 L1 in bicarbonate buffer ON at 4 °C. Plates were washed four times with wash buffer [0.05% Tween-20 (Sigma Aldrich, P1379) in PBS] and blocked with 2% bovine serum albumin (BSA, Fisher Bioreagents, Lot 170763 A) in PBS for 1 h at RT. Serum samples were serially diluted in blocking buffer and incubated for 2 h at RT followed by five washes. HRP-conjugated IgG1 (Southern Biotech, 1144-05), IgG2a (Southern Biotech, 1155-05), IgG2b (Southern Biotech, 1186-05), IgG

Fig. 7 | Design and evaluation the clearance effect of E7-GP96-Fusion protein against HPV⁺ tumors. Groups of 6- to 8-week-old female HLA-A2 transgenic mice ($n = 6$) were i.m. immunized with HPV-18 E7 vaccines adjuvanted with MF59, GP96, and E7-GP96-Fusion vaccine. Naïve mice were also included. **A**–**D** Spleens were collected 14 days after 3rd immunization and stimulated with cocktail for detection. **A** Representative flow cytometry contour plots of $CD8^+IFN\text{-}\gamma^+$/Granzyme B^+/Perforin$^+$ cells. **B** The frequency of (**A**) was analyzed. **C** Representative flow cytometry contour plots of $CD4^+IFN\text{-}\gamma^+$/Granzyme B^+/Perforin$^+$ cells. **D** The frequency of (**C**) was analyzed. **E**–**J** Analysis of the clearance effect of $CD8^+$ T cell immune response induced by E7-GP96-Fusion in an HPV$^+$ tumor challenge model. **E** Schedule of animal experiments for T cell transfer strategies in HeLa-bearing mice. **F** Tumor growth curves of HeLa tumor-bearing mice receiving intravenous transfer of different formulations every 3 days, for four immunotherapy sessions. **G** Photographs and tumor weight **H** of the collected tumor tissues on day 30. **I** Representative flow cytometry contour plots of $CD8^+$ T cells among tumor-infiltrating lymphocytes (TIL) on day 30. **J** Frequency, absolute count, and infiltration density of $CD8^+$ T cells as shown in (**I**) was analyzed. In (**A**–**J**), $n = 6$ mice per group were analyzed. The data are representative of two independent experiments with similar results. The geometric mean ± geometric SD is shown, and each data point represents an individual mouse or field. One-way ANOVA with Bonferroni correction or unpaired two-tailed t tests were conducted according to the distribution of the data. ns p å 0.05, $^*p \le 0.05$, $^{**}p \le 0.01$, $^{***}p \le 0.001$, $^{****}p \le 0.0001$.

(SouthernBiotech, 6412-05), IgA (proteintech, SA00012-7), IgE (Invitrogen, SA5-10263), IgM (Thermo Fisher, 046820) were diluted 1:5,000 in blocking buffer and incubated for 1 h, then washed seven times. Plates were developed with Pierce TMB Substrate (Thermo Scientific, 34021), and the reaction was stopped with 2 N sulfuric acid. Absorbance was measured at 450 nm using a Spectra Max microplate reader. RBD-endpoint antibody titers were calculated as reciprocal dilutions giving OD signals > average of blanks plus three times the standard deviation using GraphPad Prism. An arbitrary value of 1 was assigned to the samples with OD values below the limit of detection for which it was not possible to interpolate the titer.

Antibody-dependent cell-mediated cytotoxicity reporter bioassay

To evaluate antibody-dependent cell-mediated cytotoxicity (ADCC), Jurkat-mFcγRIII-NFAT-Luc reporter cells (Promega, M1211) were used as ADCC bioassay effector cells, and 293FT cells with stable expression of SARS-CoV-2 spike protein were used as ADCC bioassay target cells. For all ADCC assays, target cells (4.25×10^3 per well) were incubated with effector cells (7.5×10^4 per well) and serial dilutions of serum samples were performed at 37 °C for 16 h. After incubation, the relative light unit (RLU) was detected according to the instructions provided by PerkinElmer (Waltham, MA). Fold of induction (FI) was calculated as follows: FI = RLU (induced − background)/RLU (negative serum control − background).

Live SARS-CoV-2 neutralization assay

The live virus neutralization assay was conducted in a BSL-3 facility. Briefly, sera from immunized mice were 2-fold (SARS-CoV-2 neutralization assay) serially diluted and mixed with the same volume of SARS-CoV-2 (100 TCID50), incubated at 37 °C. Thereafter, 100 mL virus-serum mixture was transferred to pre-plated Vero cells in 96-well plates. Inoculated plates were incubated at 37 °C for an additional 72 h, following which the CPE of the virus was observed microscopically at 40-fold magnification. The neutralization titers were defined as the reciprocal of serum dilution required for 50% neutralization of viral infection.

Mice immunizing and viruses challenging

For SARS-CoV-2 challenge experiments, nine hACE2 transgenic mice (8-10-week-old female mice) in each group were intramuscularly immunized in a prime-boost regime. Phosphate-buffered saline (PBS) was employed in the negative control group. Two weeks post the third immunization, mice were infected with 5×10^5 TCID50 of SARS-CoV-2 XBB.1.22 via the intranasal infection. All mice were euthanized on the 3rd day following the challenge. Lung tissues were harvested for virus load detection (six mice per group) and pathological examination (three mice per group).

Histopathology analysis

Three mice in each group were euthanized on the 3rd day after infection according to standard procedures. Lung samples from challenged mice were collected and immobilized in 10% neutral buffer formaldehyde and embedded in paraffin wax. Tissue sections were treated with hematoxylin and eosin (H&E) and analyzed microscopically.

Fluorescent probe generation

RBD or L1 proteins used for flow cytometry experiments were independently conjugated to both R-APC/Cy7 and R-PE/Cy5 using Lightning-Link R-APC/Cy7 (Abcam, ab102859) and Lightning- Link R-PE/Cy5 (Abcam, ab102893) kits, following manufacturer's instructions.

ICS and immunophenotyping by flow cytometry

For the detection of cytokine secretion, the final concentration of the stimulated target protein was 20 μg/mL, the final concentration of the polypeptide or peptide library was 20 μg/mL, and the concentration of the Cocktail was used as per the instructions (BioLegend, 423303). The cells were stimulated in 96-well plates for 24 h, with 2×10^6 cells plated in each well. The Brefeldin A (Invitrogen, 00-4506-51) was added before sample collection, 4–6 h in advance.

All staining steps were carried out at 4 °C in Cell Staining Buffer (BioLegend, 420201). All the steps of cell fixation and membrane disruption are carried out using eBioscience Fixation / Permeabilization Diluent (eBioscience, 00-5223-56). The flow cytometry protocols for various types of immune cells are as follows. Among them, the antigen-APC-Cy7$^+$ antigen-PE-Cy5$^+$ gating strategy was ultimately used for antigen-specific cells.

GC B: $CD19^+Fas^+GL7^+$
MBC Precursors: $CD19^+Fas^+GL7^+CXCR4^-CD86^+$(LZ) $CCR6^+$
MBCs: $CD19^+B220^+IgD^-Fas^-CD38^+IgG1^+$/ IgG2a/2b$^+$
FDCs: $CD31^-$podoplanin$^+CD16/32^+CD21/35^+$
Tfh: $CD4^+B220^-CD44^{hi}CD62L^-CXCR5^+PD\text{-}1^+IL\text{-}21^+/IFN\text{-}\gamma^+/IL\text{-}4^+$
AIM^+CD4^+T: $CD3^+CD4^+CD137^+OX40^+$
AIM^+CD8^+T: $CD3^+CD8^+CD137^+CD69^+$

ELISPOT

A detailed protocol was previously published[8]. Briefly, multi Screen HTS IP filter plates of 0.45 μm (Millipore Sigma, MSIPS4W10) were coated with 2.5 μg/mL SARS-CoV-2 RBD or HPV18 L1 in bicarbonate buffer (35 mM NaHCO3 and 15 mM Na2CO3) ON at 4 °C. Plates were washed three times with PBS and blocked with complete DMEM for at least 1 h at 37 °C. Single cell suspensions of BM cells were serially diluted in complete DMEM with halving dilutions starting at one million cells. Following ON incubation at 37 °C and 5% CO2, plates were washed three times with 0.05% Tween-20 in PBS. Membranes were incubated with anti-IgG-HRP (Jackson Immuno Research, 115-035-003) detection antibody diluted in complete DMEM for 2 h at RT. Plates were washed three times with 0.05% Tween-20 in PBS, and spots corresponding to antigen-specific antibody-secreting cells (ASC) were developed using BD ELISPOT AEC Substrate Set (551951). Membranes were dried overnight and counted using a CTL Immunospot analyzer (Shaker Heights, OH).

Inhibitor blocking

For the prepared suspension of lymph node cells, in every 2×10^6 cells FCR blocking (Miltenyi Biotec, 130-092-575) was used at a ratio of 1:10, or TLR1 (Abcam, ab37068), TLR2 (Abcam, ab209216), TLR4 (Abcam, ab22048), and LRP1 (Abcam, ab92544) mAb were used at a ratio of 1:200 for blocking and inhibition. The blocking process was carried out

at room temperature for 1 hour. Subsequently, various flow cytometry staining studies were conducted.

Western blot and co-immunoprecipitation assay

In the early stage of the in vivo experiment, mice were immunized with a normal immune dose. Seven days after the first immunization, inguinal and axillary lymph nodes of the mice were collected, and FDC cells were sorted using flow cytometry. In the early stage of the in vitro experiment, mice were not immunized, and FDC cells were directly sorted from the lymph nodes of the limbs. The cells were incubated with 5 μg RBD, 5 μg RBD + 15 μg GP96, and 20 μg RBD-GP96-Fusion at 4 °C for 4 h respectively. Subsequently, the cells were lysed with RIPA (Beyotime, P0013B), and the cell lysate was incubated with RBD mAb (1:500, Abclonal, A23771) at a 1:100 ratio at 4 °C overnight. Protein A/G agarose was added and incubated with shaking at 4 °C for 1–2 h. For the BCR-COIP experiment, the lymph nodes of the limbs were collected from immunized mice. They were then ground to obtain a suspension, and the cells were directly lysed. Protein A/G agarose was added and incubated with shaking at 4 °C for 1–2 h. Subsequently, Western Blot analysis was performed for the above three different treatments. The primary antibodies for incubation are respectively RBD mAb (1:500, Abclonal, A23771), GRP94 (GP96) mAb (1:1000, CST, 20292 T), and LRP1 mAb (1:200, Abcam, ab92544).

The incubation ratio of the primary antibody, HPV18 L1 mAb (Abcam, ab267404), for the detection of HPV-infected cell lines in the Western Blot assay is 1:500.

Live cell imaging and analysis

Separation and isolation of GC B and FDC cells from the inguinal lymph nodes of immunized mice. LRP1 blocking monoclonal antibody (clone 761704; RnD Systems) or rat IgG2a isotype antibody (clone eBR2a; eBioscience) were added 2 h before imaging at a final concentration of 10 μg/ml. Antibody clones and concentrations were based on previously established protocols. Before imaging, GC B cells were labeled with Cell Tracker Hoechst dye and added to the FDC culture dishes at a 1:1 FDC:B-cell ratio. Cells were imaged on a Nikon A1 inverted microscope (Nikon) using a 40X objective. Images were captured every 5 min for a total of 1 or 2 h. Videos were analyzed using NIS Elements (Nikon) and ImageJ with Manual Tracking plugin. For interaction time analysis, total contact duration per GC B detected from videos was calculated based on the number of frames in which a GC B came in contact with a FDC.

Single-cell RNA sequencing and data processing

Freshly isolated $Cy5^+$ lymph node cells were sorted to > 99% purity using a BD FACS Aria III. For the scRNA-seq analysis of $Cy5^+$ sorted cells, each experimental group (including the RBD-in-Alum control) was performed in three independent biological replicates. For each replicate, draining lymph node cells were collected from six mice that had received the same treatment and pooled prior to sorting. $Cy5^+$ lymph node cells were enriched by FACS for library preparation, and scRNA-seq was performed by Shanghai Biotechnology Corporation. The final library pool was sequenced on the Illumina NovaSeq 6000 instrument using 150-base pair paired-end reads. Raw sequencing data were converted to FASTQ files and aligned to the mouse genome reference sequence (GRCH38). The 10X Genomics Cell Ranger (version 3.0.1) was used to demultiplex samples, process barcodes, and generate a digital gene-cell matrix from this data. The output was then imported into the Seurat (version 3.1.5) R toolkit for quality control and downstream analysis. Cells with less than 200 genes and cells with above 20% mitochondrial genes were removed as low-quality cells. Cells with abnormally high unique molecular identifiers or gene numbers were also identified as putative doublets and removed. The Louvain algorithm was used for the unsupervised computational analysis of scRNA-seq data.

Immunostaining for confocal analysis

A 14-mm confocal dish was placed on a 6-well plate. RAW264.7 or BMDC cells were seeded in the 6-well plate at a density of 2×10^6 cells per well and incubated for 30 min at 37 °C in a cell culture incubator. For intracellular staining in the subsequent steps, inhibitors BAFA1 or MG132 were used for blocking at a ratio of 1:200 for 2–4 hours before protein incubation. Different experimental groups were incubated with 5 μg of RBD, 5 μg of RBD + 15 μg of GP96, and 20 μg of RBD-GP96-Fusion for 1 hour. After washing twice with PBS, cells were fixed with 4% paraformaldehyde for 10 min. For subsequent staining of cell surface markers, cells were washed with PBS, while for intracellular staining, cells were washed with 0.5% PBST. A 4% BSA blocking solution was prepared and cells were blocked in a 37 °C cell culture incubator for 15 min. The primary antibody prepared with the blocking solution was added and incubated at room temperature for 3 h. The secondary antibody prepared with the blocking solution was added after washing and incubated at room temperature for 1 h. Following another round of washing, DAPI and mounting reagent were added for subsequent machine analysis. The staining dilution ratios of the antibodies were as follows: LRP1 mAb 1:200 (Abcam, ab92544), RBD mAb 1:500 (Abclonal, A23771), EEA1 mAb 1:100 (CST, 2411S), Rab7 mAb 1:100 (Abcam, ab126712), LAMP1 mAb 1:100 (CST, 9091S), Calnexin pAb 1:500 (Abcam, ab22595), RBD pAb 1:200 (SinoBiological, 40592-MP01), Anti-mouse-TRITC 1:200 (ORIGENE, ZF-0313), and Anti-rabbit-FITC 1:200 (ORIGENE, ZF-0311).

Z-stack images were generated by Imaris (ver 9.7.2). The resulting images were processed by analyzing colocalization, and the percentage of ROI colocalized for cellular membrane and cytosol were obtained respectively. In each assay, a total of 6 fields were randomly selected and quantified.

In vitro cells killing assay

Splenocytes were isolated from immunized mice on day 12 after the 3rd immunization, and collected as effector cells. The target cells (MS751) were labeled with 2.5 μM 5-(6)-carboxy-fluorescein succinimidyl ester (CFSE) dye and washed with PBS. We then seeded CFSE-labeled target cells in 100 μL complete RPMI 1640 medium into 96-well round-bottom plates. Effector cells were added to the CFSE-labeled target cells at varying ratios in 100 μL complete RPMI 1640 medium for 4–6 h at 37 °C. The dead cells were labeled with 7-AAD, and cytotoxicity of splenocytes to tumor cells was detected using flow cytometry.

Trypsin protection assay

10 μM purified RBD, GP96 and RBD-GP96-Fusion were incubated at 37 °C for 15 min. The reaction was acidified with increasing amounts of 0.1 M citrate to achieve a series of pH values from pH 7.4 to 5.0 to induce conformational changes in GP96, and incubated for additional 5 min at 37 °C. The solution was then neutralized with 0.5 M Tris (final pH 7.3). 2 μg of trypsin (TPCK [tolylsulfonyl phenylalanyl chloromethyl ketone] treated; New England Bio-Labs) were added. Digestion was carried out for 1 h at 20 °C, and terminated by the addition of 5× SDS sample loading buffer and heated at 100 °C for 10 min. The extent of GP96 or RBD-GP96-Fusion digestion was analyzed by SDS-PAGE.

BAL and lung harvest and cell Isolation

For mouse samples, spleens were collected, and tissues processed into single-cell suspension. Leukocytes were isolated from spleen by mechanical dissociation and red blood cells were lysed by lysing solution. BAL was harvested directly from euthanized mice via insertion of a 22-gauge catheter into an incision into the trachea. Hanks' Balanced Salt Solution (HBSS) was injected into the trachea and aspirated 4 times. Recovered lavage fluid was collected and BAL cells were gathered after centrifugation. To isolate intraparenchymal lung lymphoid cells, the lungs were flushed by 5 ml of prechilled HBSS into the right ventricle. When the color of the lungs changed to white, the lungs

were excised avoiding the peritracheal lymph nodes. Lungs were then removed, washed in HBSS and cut into 3-mm pieces, and incubated in Iscove's Modified Dulbecco's Medium containing 1 mg/ml collagenase IV (Sigma) for 30 min at 37 °C on a rotary agitator (~60 rpm). Any remaining intact tissue was disrupted by passage through a 21-gauge needle. Tissue fragments and majority of the dead cells were removed by a 250-micrometer mesh screen, and cells were collected after centrifugation.

Induction culture of BMDC cells

BMDCs were obtained as previously described[63]. Briefly, bone marrow cells were harvested from the femur and tibia of 5–7-weekold mice, and red blood cells were depleted using red blood lysis buffer. The bone marrow cell suspensions were cultured in complete RPMI medium containing 10% heat inactivated FBS, 20 ng/mL granulocyte macrophage colony-stimulating factor (GM-CSF), 10 ng/mL interleukin-4 (IL-4), and 50 μM 2-mercaptoethanol (Sigma-Aldrich, St. Louis, MO, USA). All cytokines were purchased from PeproTech (Rocky Hill, NJ, USA). After 7 days of culture, nonadherent BMDCs were generated and collected.

Peptide synthesis and epitope prediction

The 8-10-mer epitope was predicted using long peptides from the website NetMHC-4.0 (https://services.healthtech.dtu.dk/services/NetMHC-4.0/). The strong binding threshold and weak binding threshold are 0.5% Rank and 2% Rank, respectively. All peptides were synthesized by GenScript (Nanjing, China) and were more than 95% pure.

Quantitative detection of HPV-L1 mouse antibodies by ELISA

Serum from immunized mice was collected and the levels of HPV L1 antibodies were quantitatively detected using the following ELISA kits: Mouse Anti-Human Papilloma Virus 16 late protein L1 IgG (HPV16L1) ELISA kit, quantitative, 96 tests (Alpha Diagnostic International, 550-316-PMG); Mouse Anti-Human Papilloma Virus 18 late protein L1 IgG (HPV18L1) ELISA kit, quantitative, 96 tests (Alpha Diagnostic International, 550-318-PMG); Mouse Anti-Human Papilloma Virus 31 late protein L1 IgG (HPV31L1) ELISA kit, quantitative, 96 tests (Alpha Diagnostic International, 550-331-PMG); Mouse Anti-Human Papilloma Virus 45 late protein L1 IgG (HPV45L1) ELISA kit, quantitative, 96 tests (Alpha Diagnostic International, 550-345-PMG).

Animal tumor model and adoptive therapy

The subcutaneous HeLa xenograft model was established by inoculating HeLa cells (2×10^6 cells) into the right foreleg of female BALB/c nude mice (4- to 5-week-old, 18–22 g). At four days after tumor cell inoculation, the tumor-bearing mice were randomly divided into four groups and immunized intravenously in the tail with 3×10^6 T cells isolated from the spleens of different immunization treatment groups four times at 3-day intervals. Adoptive T cells were enriched using a $CD8^+$ T cell isolation kit (Stemcell, 19853). Tumor growth was monitored with calipers every other day, and the tumor volume was calculated using the following formula: volume = length × width^2 × 0.5. Mice were monitored daily for general health and signs of distress. In accordance with the guidelines of our Institutional Animal Care and Use Committee (IACUC), the following humane endpoints were strictly adhered to, and any animal reaching one of these criteria was euthanized immediately:

Tumor burden: The tumor volume exceeded 1500 mm^3.

Ulceration or necrosis: The tumor showed signs of severe ulceration or necrosis.

Body condition: A loss of > 20% of initial body weight.

Behavioral signs: Signs of severe pain, distress, or lethargy that inhibited the animal from accessing food or water.

Physical impairment: The tumor size interfered with locomotion or normal bodily functions.

Euthanasia was performed by cervical dislocation under deep anesthesia induced by isoflurane inhalation, a method approved by our IACUC.

Statistical analysis

KD values for SPR assays were calculated by the software BIA evaluation Version 4.1 (GE Healthcare), using 1:1 binding model. The values shown are mean ± SD of two independent experiments. Details can be found in figures legends.

GraphPad Prism version 8 was used to conduct all statistical analysis. Shapiro-Wilk and Kolmogorov-Smirnov tests were performed to establish the normal distribution of the data. The significance of differences among groups was calculated according to the distribution of the data using unpaired one-way ANOVA with Bonferroni correction or two-tailed Mann-Whitney U tests. Correlations were determined using Spearman's rank coefficient with a 95% confidence interval. Rare samples that presented technical issues in the flow cytometry staining were excluded from the analysis. The precise number of samples analyzed in each graph is reported in figure legends. The specific p-value results of each statistical analysis are presented in the "source-data" file. Statistical significance was set at the critical values of $p < 0.05$ (*), $p < 0.01$ (**), $p < 0.001$ (***), and $p < 0.0001$ (****).

Reporting summary

Further information on research design is available in the Nature Portfolio Reporting Summary linked to this article.

Data availability

The scRNA-seq data generated in this study have been deposited in the National Center for Biotechnology Information Sequence Read Archive (NCBI SRA) under accession number PRJNA1195897. A total of six samples were obtained. Source data are provided with this paper.

References

1. Forni, G. & Mantovani, A. COVID-19 Commission of Accademia Nazionale dei Lincei, Rome. COVID-19 vaccines: where we stand and challenges ahead. *Cell Death Differ.* **28**, 626–639 (2021).
2. Zhao, F., Zai, X., Zhang, Z., Xu, J. & Chen, W. Challenges and developments in universal vaccine design against SARS-CoV-2 variants. *NPJ vaccines* **7**, 167 (2022).
3. Poletti, P. Kinetics of neutralising antibodies against SARS-CoV-2 variants. *Lancet Infect. Dis. S* **1473**, 00513–00519 (2024).
4. Bertoletti, A., Le Bert, N., Qui, M. & Tan, A. T. SARS-CoV-2-specific T cells in infection and vaccination. *Cell Mol. Immunol.* **18**, 2307–2312 (2021).
5. Mendonça, S. A., Lorincz, R., Boucher, P. & Curiel, D. T. Adenoviral vector vaccine platforms in the SARS-CoV-2 pandemic. *NPJ vaccines* **6**, 97 (2021).
6. Dai, L. et al. A Universal Design of Betacoronavirus Vaccines against COVID-19, MERS, and SARS. *Cell* **182**, 722–733.e11 (2020).
7. Lederer, K. et al. SARS-CoV-2 mRNA vaccines foster potent antigen-specific germinal center responses associated with neutralizing antibody generation. *Immunity* **53**, 1281–1295.e5 (2020).
8. Laczkó, D. et al. A single immunization with nucleoside-modified mrna vaccines elicits strong cellular and humoral immune responses against SARS-CoV-2 in Mice. *Immunity* **53**, 724–732.e7 (2020).
9. Tian, J. H. et al. SARS-CoV-2 spike glycoprotein vaccine candidate NVX-CoV2373 immunogenicity in baboons and protection in mice. *Nat. Commun.* **12**, 372 (2021).
10. Shams, N. et al. An overview of the types of adjuvants used in the vaccination industry and their mechanisms of action. *Viral Immunol.* **37**, 324–336 (2024).
11. Yang, J. et al. A vaccine targeting the RBD of the S protein of SARS-CoV-2 induces protective immunity. *Nature* **586**, 572–577 (2020).

12. Moss, P. The T cell immune response against SARS-CoV-2. *Nat. Immunol.* **23**, 186–193 (2022).
13. Liu, Y. et al. Cross-neutralization and cross-protection among SARS-CoV-2 viruses bearing different variant spikes. *Signal Transduct. Target Ther.* **7**, 285 (2022).
14. Peng, Y. et al. Broad and strong memory CD4+ and CD8+ T cells induced by SARS-CoV-2 in UK convalescent individuals following COVID-19. *Nat. Immunol.* **21**, 1336–1345 (2020).
15. Ju, Y. et al. Heat shock protein gp96 adjuvant induces T cell responses and cross-protection to a split influenza vaccine. *Vaccine* **32**, 2703–2711 (2014).
16. Wang, S. et al. Heat shock protein gp96 enhances humoral and T cell responses, decreases Treg frequency and potentiates the anti-HBV activity in BALB/c and transgenic mice. *Vaccine* **29**, 6342–6351 (2011).
17. Berwin, B., Hart, J. P., Pizzo, S. V. & Nicchitta, C. V. Cutting edge: CD91-independent cross-presentation of GRP94(gp96)-associated peptides. *J. Immunol.* **168**, 4282–4286 (2002).
18. Singh-Jasuja, H. et al. The heat shock protein gp96 induces maturation of dendritic cells and down-regulation of its receptor. *Eur. J. Immunol.* **30**, 2211–2215 (2000).
19. Zhang, H. et al. Broadly protective CD8+ T cell immunity to highly conserved epitopes elicited by heat shock protein gp96-adjuvanted influenza monovalent split vaccine. *J. Virol. Nov. 23* **95**, e0175021 (2021).
20. Li, C., Du, Y., Zhang, Y. & Ji, N. Immunotherapy with heat shock protein 96 to treat gliomas. *Chin. Neurosurg. J.* **6**, 31 (2020).
21. Lin, M. J. et al. Cancer vaccines: the next immunotherapy frontier. *Nat. Cancer* **3**, 911–926 (2022).
22. Padula, L., Fisher, E. & Strbo, N. All for one and one for all": the secreted heat shock protein gp96-Ig based vaccines. *Cells* **13**, 72 (2023).
23. Huck, J. D., Que, N. L., Hong, F., Li, Z. & Gewirth, D. T. Structural and Functional Analysis of GRP94 in the Closed State Reveals an Essential Role for the Pre-N Domain and a Potential Client-Binding Site. *Cell Rep.* **20**, 2800–2809 (2017).
24. Zhu, F. C. et al. Safety and immunogenicity of human papillomavirus-16/18 AS04-adjuvanted vaccine in healthy Chinese females aged 15 to 45 years: a phase I trial. *Chin. J. Cancer* **30**, 559–564 (2011).
25. Bryan, J. T. Developing an HPV vaccine to prevent cervical cancer and genital warts. *Vaccine* **25**, 3001–3006 (2007).
26. Zhang, W. Y. et al. Revolutionizing adjuvant development: harnessing AI for next-generation cancer vaccines. *Front Immunol.* **15**, 1438030 (2024).
27. Wang, M. et al. A human monoclonal antibody targeting the monomeric N6 neuraminidase confers protection against avian H5N6 influenza virus infection. *Nat. Commun.* **15**, 8871 (2004).
28. He, Q. et al. Immunogenicity and protective efficacy of a recombinant protein subunit vaccine and an inactivated vaccine against SARS-CoV-2 variants in non-human primates. *Signal Transduct. Target Ther.* **7**, 69 (2022).
29. Mathew, N. R. et al. Single-cell BCR and transcriptome analysis after influenza infection reveals spatiotemporal dynamics of antigen-specific B cells. *Cell Rep.* **35**, 109286 (2021).
30. Nguyen, H. T. T., Guevarra, R. B., Magez, S. & Radwanska, M. Single-cell transcriptome profiling and the use of AID deficient mice reveal that B cell activation combined with antibody class switch recombination and somatic hypermutation do not benefit the control of experimental trypanosomosis. *PLoS Pathog.* **17**, e1010026 (2021).
31. Zhang, Y. et al. Microbiota-mediated shaping of mouse spleen structure and immune function characterized by scRNA-seq and Stereo-seq. *J. Genet Genomics* **50**, 688–701 (2023).
32. Pušnik, J. et al. Memory B cells targeting SARS-CoV-2 spike protein and their dependence on CD4+ T cell help. *Cell Rep.* **35**, 109320 (2021).
33. Chu, Y. et al. CpG adjuvant enhances humoral and cellular immunity against OVA in different degrees in BALB/c, C57BL/6J, and C57BL/6N mice. *Int Immunopharmacol.* **138**, 112593 (2024).
34. Cheng, H. W. et al. Origin and differentiation trajectories of fibroblastic reticular cells in the splenic white pulp. *Nat. Commun.* **10**, 1739 (2019).
35. Aung, A. et al. Low protease activity in B cell follicles promotes retention of intact antigens after immunization. *Science* **379**, eabn8934 (2023).
36. Heesters, B. A., Myers, R. C. & Carroll, M. C. Follicular dendritic cells: dynamic antigen libraries. *Nat. Rev. Immunol.* **14**, 495–504 (2014).
37. Krimpenfort, L. T., Degn, S. E. & Heesters, B. A. The follicular dendritic cell: At the germinal center of autoimmunity? *Cell Rep.* **43**, 113869 (2024).
38. Heesters, B. A., Van der Poel, C. E. & Carroll, M. C. Follicular dendritic cell isolation and loading of immune complexes. *Methods Mol. Biol.* **1623**, 105–112 (2017).
39. El Shikh, M. E. M., El Sayed, R. & Pitzalis, C. Isolation and characterization of mouse and human follicular dendritic cells. *Methods Mol. Biol.* **1623**, 113–123 (2017).
40. Binder, R. J., Han, D. K. & Srivastava, P. K. CD91: a receptor for heat shock protein gp96. *Nat. Immunol.* **1**, 151–155 (2000).
41. Staron, M. et al. gp96, an endoplasmic reticulum master chaperone for integrins and Toll-like receptors, selectively regulates early T and B lymphopoiesis. *Blood* **115**, 2380–2390 (2010).
42. Basu, S., Binder, R. J., Ramalingam, T. & Srivastava, P. K. CD91 is a common receptor for heat shock proteins gp96, hsp90, hsp70, and calreticulin. *Immunity* **14**, 303–313 (2001).
43. Zhuang, Z. et al. Correction: Mapping and role of T cell response in SARS-CoV-2-infected mice. *J. Exp. Med* **218**, e2020218710052021c (2021c).
44. Habel, J. R. et al. Suboptimal SARS-CoV-2-specific CD8+ T cell response associated with the prominent HLA-A*02:01 phenotype. *Proc. Natl. Acad. Sci. USA* **117**, 24384–24391 (2020).
45. Deng, J. et al. Identification of HLA-A2 restricted CD8+ T cell epitopes in SARS-CoV-2 structural proteins. *J. Leukoc. Biol.* **110**, 1171–1180 (2021).
46. Fisher, E. et al. Induction of SARS-CoV-2 Protein S-Specific CD8+ T Cells in the Lungs of gp96-Ig-S Vaccinated Mice. *Front Immunol.* **11**, 602254 (2021).
47. Meng, F. et al. Fc-empowered exosomes with superior epithelial layer transmission and lung distribution ability for pulmonary vaccination. *Bioact. Mater.* **42**, 573–586 (2024).
48. Ruane, D. et al. Lung dendritic cells induce migration of protective T cells to the gastrointestinal tract. *J. Exp. Med* **210**, 1871–1888 (2013).
49. Jung, J. H. et al. SARS-CoV-2-specific T cell memory is sustained in COVID-19 convalescent patients for 10 months with successful development of stem cell-like memory T cells. *Nat. Commun.* **2**, 4043 (2021).
50. Gattinoni, L. et al. Wnt signaling arrests effector T cell differentiation and generates CD8+ memory stem cells. *Nat. Med* **15**, 808–813 (2009).
51. Buck, C. B., Day, P. M. & Trus, B. L. The papillomavirus major capsid protein L1. *Virology* **445**, 169–174 (2013).
52. Baidya, S., Das, R., Kabir, M. G. & Arifuzzaman, M. Epitope design of L1 protein for vaccine production against Human Papilloma Virus types 16 and 18. *Bioinformation* **13**, 86–93 (2017).
53. Xu, C., Liu, W., Hu, Y., Li, W. & Di, W. Bioinspired tumor-homing nanoplatform for co-delivery of paclitaxel and siRNA-E7 to HPV-related cervical malignancies for synergistic therapy. *Theranostics* **10**, 3325–3339 (2020).
54. Qin, L. et al. GPC3 and PEG10 peptides associated with placental gp96 elicit specific T cell immunity against hepatocellular carcinoma. *Cancer Immunol. Immunother.* **72**, 4337–4354 (2023).

55. Binder, R. J., Anderson, K. M., Basu, S. & Srivastava, P. K. Cutting edge: heat shock protein gp96 induces maturation and migration of CD11c+ cells in vivo. *J. Immunol.* **165**, 6029–6035 (2000).
56. Crane, C. A. et al. Individual patient-specific immunity against high-grade glioma after vaccination with autologous tumor derived peptides bound to the 96 KD chaperone protein. *Clin. Cancer Res* **19**, 205–214 (2013).
57. Testori, A. et al. Phase III comparison of vitespen, an autologous tumor-derived heat shock protein gp96 peptide complex vaccine, with physician's choice of treatment for stage IV melanoma: the C-100-21 Study Group. *J. Clin. Oncol.* **26**, 955–962 (2008).
58. Li, Y. et al. Hansenula polymorpha expressed heat shock protein gp96 exerts potent T cell activation activity as an adjuvant. *J. Biotechnol.* **151**, 343–349 (2011).
59. Kubo, M. T follicular helper and TH2 cells in allergic responses. *Allergol. Int* **66**, 377–381 (2017).
60. Feng, H. et al. Pathogen-associated T follicular helper cell plasticity is critical in anti-viral immunity. *Sci. China Life Sci.* **65**, 1075–1090 (2022).
61. Weinstein, J. S. et al. STAT4 and T-bet control follicular helper T cell development in viral infections. *J. Exp. Med* **215**, 337–355 (2018).
62. Sun, L. et al. A new unconventional HLA-A2-restricted epitope from HBV core protein elicits antiviral cytotoxic T lymphocytes. *Protein Cell* **5**, 317–327 (2014).
63. Zhang, M. et al. Splenic stroma drives mature dendritic cells to differentiate into regulatory dendritic cells. *Nat. Immunol.* **5**, 1124–1133 (2004).

Acknowledgements

We would like to thank Tong Zhao (Institute of Microbiology, CAS) for FACS sorting and technical help. We thank Xiaolan Zhang (Institute of Microbiology, CAS) for performing the confocal laser scanning microscopy and SIM imaging. We thank Jingfang Liu (Institute of Microbiology, CAS) for assistance in locating disulfide bonds, Jingnan Liang (Institute of Microbiology, CAS) for help with transmission electron microscopy, Wei Zhang (Institute of Microbiology, CAS) and Zheng Fan (Institute of Microbiology, CAS) for their assistance with BIACORE and protein thermal stability testing. We thank Yi Shi (Institute of Microbiology, CAS) for providing the Jurkat-mFcγRIII-NFAT-Luc reporter cells. We also thank Yunpeng Liu (Institute of Laboratory Animals Science, CAMS & PU) and the staff of the Biosafety Level 3 (BSL-3) equipped laboratories at Institute of Laboratory Animals Science, CAMS & PU for providing SARS-CoV-2 virus and assistance during animal experiments. This work was supported by grants from National Key R&D Program of China (2022YFC2304203, 2022YFC2304202), grants from the National Natural Science Foundation of China (32070163, 32470997). It was also funded by the Guangxi Natural Science Foundation (2024GXNSFAA010118), program for scientific research start-up funds of The First People's Hospital of Nanning (YN2023003).

Author contributions

S.M., F.C., and X.L. conceived the project. F.C., B.W. and X.Z. performed the experiments. X.L. and R.W. analyzed the data. Z.W., H.W., R.L., C.X. and Y.J.assisted with FACS staining and data analysis. F.C. and S.M. wrote the manuscript.

Competing interests

The authors declare no competing interests.

Additional information

Supplementary information The online version contains supplementary material available at https://doi.org/10.1038/s41467-025-67092-x.

Correspondence and requests for materials should be addressed to Rongguo Wei, Xin Li or Songdong Meng.

Peer review information *Nature Communications* thanks Abeer Obaid and the other, anonymous, reviewer(s) for their contribution to the peer review of this work. A peer review file is available.